

Weak universality, quantum many-body scars and anomalous infinite-temperature autocorrelations in a one-dimensional spin model with duality

Adithi Udupa¹, Samudra Sur¹, Arnab Sen² and Diptiman Sen^{1,3}

¹Center for High Energy Physics, Indian Institute of Science, Bengaluru 560012, India

²School of Physical Sciences, Indian Association for the Cultivation of Science, Jadavpur, Kolkata 700032, India

³Department of Physics, Indian Institute of Science, Bengaluru 560012, India

We study a one-dimensional spin-1/2 model with three-spin interactions and a transverse magnetic field h . The model is known to have a $Z_2 \times Z_2$ symmetry, and a duality between h and $1/h$. The self-dual point at $h = 1$ is a quantum critical point with a continuous phase transition. We compute the critical exponents z , β , γ and ν , and the central charge c numerically using exact diagonalization. We find that both z and c are equal to 1, implying that the critical point is governed by a conformal field theory with a marginal operator. The three-spin model exhibits Ashkin-Teller criticality with an effective coupling that is intermediate between four-state Potts model and two decoupled transverse field Ising models. An energy level spacing analysis shows that the model is not integrable. For a system with an even number of sites and periodic boundary conditions, there are exact mid-spectrum zero-energy eigenstates whose number grows exponentially with the system size. A subset of these eigenstates have wave functions which are independent of the value of h and have unusual entanglement structure; hence these can be considered to be quantum many-body scars. The number of such quantum scars scales at least linearly with system size. Finally, we study the infinite-temperature autocorrelation functions at sites close to one end of an open system. We find that some of the autocorrelators relax anomalously in time, with pronounced oscillations and very small decay rates if $h \gg 1$ or $h \ll 1$. If h is close to the critical point, the autocorrelators decay quickly to zero except for an autocorrelator at the end site.

I. INTRODUCTION

The well-known transverse field Ising model (TFIM) in one dimension has been studied extensively over many years¹⁻³. The Hamiltonian of the model consists of two-spin interactions (with strength set equal to 1) and a transverse magnetic field with strength h ,

$$H_2 = - \sum_{j=1}^L [\sigma_j^z \sigma_{j+1}^z + h \sigma_j^x], \quad (1)$$

where σ_j^a denote the Pauli matrices at site j corresponding to a spin-1/2 degree of freedom, and we are considering a system with L sites and periodic boundary conditions (PBC). The model has a Z_2 symmetry since an operator $D = \prod_{j=1}^L \sigma_j^x$ commutes with the Hamiltonian. The model is known to have a quantum phase transition at a critical point given by $h = 1$. It has a ordered phase for $h < 1$ with a finite magnetization (the Z_2 symmetry is spontaneously broken in this phase), and a disordered phase for $h > 1$ with zero magnetization. It also exhibits duality^{4,5} and the self-dual point $h = 1$ is the quantum critical point. The critical point is known to be described by a conformal field theory with $c = 1/2$ and certain critical exponents which are known analytically⁶.

Generalizations of the TFIM with p -spin interactions with duality have been studied using mean-field theories and perturbative calculations⁷⁻¹², with the TFIM corresponding to the case $p = 2$. It is of particular interest to take a close look at what happens in the next simplest case $p = 3$ where the order of phase transition in literature has been debated. We study this case numerically using exact diagonalization (ED) and look at the quantum criticality in this system at the self-dual point which is again given by $h = 1$. Another motivation for studying the case of $p = 3$ is that a Hamiltonian of this

form may be engineered using optical lattices either with two atomic species¹³ or with polar molecules driven by microwave fields¹⁴. We note that for the model with $p = 4$, it is not clear whether the transition at the self-dual point is first-order or continuous, while models with $p \geq 5$ are believed to have a first-order transition at the self-dual point⁸⁻¹⁰.

The three-spin ($p = 3$) model is a candidate for interesting high-energy behavior as well. For an even number of spins and periodic boundary conditions (PBC), this model satisfies an index theorem¹⁵ that results in the presence of an exponentially large number (in system size) of exact mid-spectrum zero energy eigenstates. Since these states are degenerate in energy, any linear combination of these is also an eigenstate of the system. Recent works¹⁶⁻²⁰ have shown that this freedom allows for the possibility of creating mid-spectrum eigenstates which violate the eigenvalue thermalization hypothesis (ETH) by possessing very low entanglement entropy compared to the expected thermal entropy. These eigenstates can be classified as quantum many-body scars²¹⁻²⁸. It would be interesting to see if the three-spin model hosts such scar states in the middle of the energy spectrum. Finally, we would like to examine if infinite-temperature autocorrelation functions in open chains show anomalous behaviors as a function of time for this model. A motivation to do so is provided by the observation of infinite (long) coherence times for boundary spins for the TFIM without (with) integrability-breaking perturbations due to the presence of a strong zero mode (an almost strong zero mode) that commutes (almost commutes) with the Hamiltonian²⁹⁻³³. While the TFIM can be mapped to free fermions by the standard Jordan-Wigner transformations, the perturbed TFIM has additional four-fermion interactions. It is not known if the three-spin model has analogous (almost) strong zero modes. A study of the autocorrelators near the ends of a long system may possibly shed light on this.

The plan of this paper is as follows. In Sec. II we present

the Hamiltonian of the model with three-spin interactions and its symmetries. We find that the model has a $Z_2 \times Z_2$ symmetry which leads to some degeneracies in the energy spectrum of a system with PBC. In Sec. III we discuss the duality of the model. While the duality is easy to show for an infinite-sized system, we discover that the existence of a duality is a subtle issue for finite-sized systems with PBC. In Sec. IV we make a detailed study of the criticality properties of the model at the self-dual point given by $h = 1$. Finite-size scaling is used to first confirm that there is a critical point at $h = 1$ and then to compute the dynamical critical exponent z , the order parameter exponent β , the magnetic susceptibility exponent γ , and the correlation length exponent ν . We find that $z = 1$ suggesting that the low-energy sector of the model at $h = 1$ has conformal invariance. We then determine the central charge c and find that it is close to 1. Next, we observe that although the values of β , γ and ν for the two-spin and three-spin models are different from each other, the ratios β/ν and γ/ν are the same in the two models. This suggests that there is a weak universality³⁴ and the three-spin model lies on the Ashkin-Teller (AT) line, just like two copies of the TFIM and the four-state Potts model. Using the numerically computed value of ν for the three-spin model, we estimate the location of this model on the AT line of critical points.

In Sec. V, we study the energy level spacing statistics to determine if the three-spin model is integrable. We find that the level spacing statistics has the form of the Gaussian orthogonal ensemble, and hence the model is non-integrable. Next, we find that the model has an exponentially large number of mid-spectrum zero-energy eigenstates. Further, we find that the zero-energy eigenstates are of two types which we call Type-I and Type-II. The Type-I states are simultaneous zero-energy eigenstates of the two parts of the Hamiltonian (the three-spin interaction and the transverse field) and consequently stay unchanged as a function of h , thus violating the ETH. Hence they qualify as quantum many-body scars. We give exact expressions for a subset of these Type-I states in terms of *emergent* singlets and triplets which shows that their number increases at least linearly with system size. In Sec. VI, we study the infinite-temperature autocorrelation function at sites close to one end of a large system and in the bulk with open boundary conditions; the purpose of this study is to understand if there are any states which can be interpreted as the end modes of a semi-infinite system. We find that far from the critical point, at either $h \ll 1$ or $h \gg 1$, some of the autocorrelators show an anomalous behavior in that they oscillate and also decay very slowly with time. We provide a qualitative understanding of the oscillatory behavior using perturbation theory. For values of h close to the critical point, the infinite-temperature autocorrelators decay quickly to zero except for a particular autocorrelator at the end site. In Sec. VII we summarize our main results and point out some directions for future research.

We would like to mention here that several other one-dimensional models with multispin interactions have been studied over the years, and they show a wide variety of unusual features^{35–37}. Our work makes a contribution to this interesting area of research.

II. THE MODEL AND ITS SYMMETRIES

The Hamiltonian of the three-spin model is given by^{7–12}

$$H_3 = - \sum_{j=1}^L [\sigma_j^z \sigma_{j+1}^z \sigma_{j+2}^z + h \sigma_j^x], \quad (2)$$

where σ_j^a (where $a = x, y, z$) denotes the Pauli matrices at site j , and we assume PBC so that $\sigma_{L+1}^a = \sigma_1^a$ and $\sigma_{L+2}^a = \sigma_2^a$.

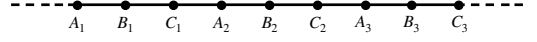


FIG. 1: The lattice for the Hamiltonian H_3 with three sublattices A, B and C are shown here. The symmetry operators are defined with respect to these sublattices in Eq. (3).

Unlike the case of TFIM, we do not have a Z_2 symmetry in this model. However we have three operators D_1 , D_2 and D_3 which commute with the Hamiltonian H_3 in Eq. (2). If the system size L is a multiple of 3, we can divide the lattice into three sublattices A, B and C as shown in Fig. 1. The three operators for this system are then defined

$$\begin{aligned} D_1 &= \prod_{j=1}^{L/3} \sigma_x^{A_j} \sigma_x^{B_j}, \\ D_2 &= \prod_{j=1}^{L/3} \sigma_x^{B_j} \sigma_x^{C_j}, \\ D_3 &= \prod_{j=1}^{L/3} \sigma_x^{C_j} \sigma_x^{A_j}. \end{aligned} \quad (3)$$

These satisfy the constraint $D_1 D_2 D_3 = I$. Thus we have four decoupled sectors corresponding to the different allowed values of these operators; $(D_1, D_2, D_3) = (1, 1, 1), (1, -1, -1), (-1, 1, -1)$ and $(-1, -1, 1)$. Thus this model has $Z_2 \times Z_2$ symmetry. All the four sectors have equal number of states. We also notice that the operator $C = \prod_{j=1}^L \sigma_y$ anticommutes with the Hamiltonian. Hence for every state $|\psi\rangle$ with energy E , there is a state $C|\psi\rangle$ with energy $-E$ due to which the spectrum of this model has a $E \rightarrow -E$ symmetry.

With PBC the system also has translation symmetry. If the translation operator is given by U , then we can see from Eq. (3), that

$$\begin{aligned} U D_1 U^{-1} &= D_2, \\ U D_2 U^{-1} &= D_3, \\ U D_3 U^{-1} &= D_1. \end{aligned} \quad (4)$$

We can further see that a combination of these three operators $D' = D_1 + \omega D_2 + \omega^2 D_3$ where ω is the cube root of unity, transforms into $e^{-i2\pi/3}(D_1 + \omega D_2 + \omega^2 D_3)$ upon translation by one site. This is because $U(D_1 + \omega D_2 + \omega^2 D_3)U^{-1} = \omega^2(D_1 + \omega D_2 + \omega^2 D_3)$. This means that for a state $|\psi_k\rangle$ with momentum k , that is, $U|\psi_k\rangle = e^{ik}|\psi_k\rangle$, we have a state $(D_1 + \omega D_2 + \omega^2 D_3)|\psi_k\rangle = e^{-i2\pi/3}e^{ik}|\psi_k\rangle = |\psi_{k-2\pi/3}\rangle$ with momentum $k - 2\pi/3$. Similarly, we have a state $(D_1 + \omega^{-1} D_2 + \omega^{-2} D_3)|\psi_k\rangle$ for which the momentum

is $k+2\pi/3$. Since the D operators commute with the Hamiltonian, the states $|\psi_k\rangle$, $|\psi_{k-2\pi/3}\rangle$ and $|\psi_{k+2\pi/3}\rangle$ are degenerate. However in the sector $(D_1, D_2, D_3) = (1, 1, 1)$, the operators $D_1 + \omega D_2 + \omega^2 D_3$ and $D_1 + \omega^2 D_2 + \omega D_3$ give zero when they act on a state $|\psi_k\rangle$. Therefore the states belonging to this sector do not have a degenerate partner. Thus in the entire spectrum, three-fourths of the states have an exact three-fold degeneracy whereas the other one-fourth belonging to the sector $(1, 1, 1)$ has no degeneracy. We also have a parity symmetry in this system. For an even system size, we can define parity as a mirror reflection about the middle bond. The parity operator then takes the operator $D_1 \rightarrow D_2$ and $D_2 \rightarrow D_1$ and keeps D_3 unchanged. Thus, for a system with open boundary conditions which breaks translation symmetry, we can still have degeneracies coming from parity symmetry. These come from the states in sectors $(D_1, D_2, D_3) = (1, -1, -1)$ and $(-1, 1, -1)$ as they go to a different sector under parity.

III. DUALITY OF THE MODEL

Just like the TFIM, the three-spin model also exhibits duality on an *infinitely large* system. We show this by starting from the original lattice with sites labeled by an integer j which goes from $-\infty$ to $+\infty$. Then the sites of dual lattice also lie at j . (This is in contrast to the TFIM where the sites of the dual lattice lie at $j + 1/2$). The transformation of the Pauli matrices going from the original lattice σ_j^a to the dual lattice $\tilde{\sigma}_j^a$ is given by

$$\begin{aligned}\tilde{\sigma}_{j+1}^x &= \sigma_j^z \sigma_{j+1}^z \sigma_{j+2}^z, \\ \tilde{\sigma}_{j-1}^z \tilde{\sigma}_j^z \tilde{\sigma}_{j+1}^z &= \sigma_j^x.\end{aligned}\quad (5)$$

The Hamiltonian on the dual lattice then takes the form

$$\tilde{H}_3 = - \sum_{j=-\infty}^{\infty} [\tilde{\sigma}_{j+1}^x + h \tilde{\sigma}_{j-1}^z \tilde{\sigma}_j^z \tilde{\sigma}_{j+1}^z]. \quad (6)$$

Thus going from H_3 to \tilde{H}_3 , the transverse field h gets mapped to $1/h$. The self-dual point lies at $h = 1/h$. Hence, if H_3 (or \tilde{H}_3) has a phase transition it must occur at $|h| = 1$.

We will now examine if duality also holds for a *finite* system with PBC as described in Eq. (2). Clearly, we would like both the original and dual lattices to have the same number of sites, L , and the number of states should be 2^L in both cases. The latter can only happen if the Pauli operators are independent operators on different sites on both the lattices. The first equation in Eq. (5) and the fact that $(\sigma_j^z)^2 = 1$ for all j imply that

$$\begin{aligned}\tilde{\sigma}_1^x \tilde{\sigma}_2^x \tilde{\sigma}_4^x \tilde{\sigma}_5^x \cdots \tilde{\sigma}_{L-2}^x \tilde{\sigma}_{L-1}^x &= I, \\ \text{and } \tilde{\sigma}_2^x \tilde{\sigma}_3^x \tilde{\sigma}_5^x \tilde{\sigma}_6^x \cdots \tilde{\sigma}_{L-1}^x \tilde{\sigma}_L^x &= I\end{aligned}\quad (7)$$

if L is a multiple of 3. Hence there are two constraints on the $\tilde{\sigma}_j^x$ operators, implying that the eigenvalues of the operators cannot take all possible values independently of each other. To put it differently, the two constraints mean that the number

of states in the dual system is 2^{L-2} rather than 2^L . We reach a similar conclusion for the original system by using the second equation in Eq. (5). We therefore conclude that duality does not hold for a finite system with PBC if L is a multiple of 3. It turns out that duality does hold if L is *not* a multiple of 3 as the Pauli operators do not satisfy any constraints on either the original lattice or the dual lattice in that case. (Note, however, that the operators D_j defined in Sec. II do not exist if L is not a multiple of 3). Next, duality implies that there must be a unitary operator U_D which relates the states of the original and dual lattices. Let us write the Hamiltonian in Eq. (2) in the form

$$\begin{aligned}H_3 &= -Z - hX, \\ \text{where } Z &= \sum_{j=1}^L \sigma_j^z \sigma_{j+1}^z \sigma_{j+2}^z, \\ X &= \sum_{j=1}^L \sigma_j^x,\end{aligned}\quad (8)$$

and similarly

$$\tilde{H}_3 = -\tilde{X} - h\tilde{Z}. \quad (9)$$

Then there must be a unitary operator U_D such that $U_D X U_D^{-1} = \tilde{Z}$ and $U_D Z U_D^{-1} = \tilde{X}$. This means that at the self-dual point $h = 1$, if $|\psi_n\rangle$ is an eigenstate of H_3 with eigenvalue E_n , and $|\tilde{\psi}_n\rangle = U_D |\psi_n\rangle$ is an eigenstate of \tilde{H}_3 with the same eigenvalue, we must have

$$\langle \psi_n | X | \psi_n \rangle = \langle \tilde{\psi}_n | \tilde{Z} | \tilde{\psi}_n \rangle = \langle \psi_n | Z | \psi_n \rangle, \quad (10)$$

where the equality $\langle \tilde{\psi}_n | \tilde{Z} | \tilde{\psi}_n \rangle = \langle \psi_n | Z | \psi_n \rangle$ is a consequence of self-duality. Since $\langle \psi_n | (-X - Z) | \psi_n \rangle = E_n$, Eq. (10) implies that

$$\langle \psi_n | X | \psi_n \rangle = -\frac{E_n}{2}. \quad (11)$$

at $h = 1$. A test of this relation will be discussed in Appendix A.

Before ending this section, we note that it is not useful to perform a Jordan-Wigner transformation from spin-1/2's to spinless fermions for this model because there are three-spin terms in the Hamiltonian. The Jordan-Wigner transformation maps σ_j^x to the occupation number $c_j^\dagger c_j$ of fermions at site j , and σ_j^z to $c_j + c_j^\dagger$ times a string of σ_n^x operators running from $n = -\infty$ to $j-1$ (for an infinitely large system). The presence of the three-spin term $\sigma_j^z \sigma_{j+1}^z \sigma_{j+2}^z$ in the Hamiltonian implies there will be an infinitely long string of σ_n^x operators left over which does not cancel with anything. Thus this model cannot be solved by fermionizing since the fermionic Hamiltonian will have highly non-local terms. We will henceforth analyze the model numerically. In the next section, we will carry out ED calculations to confirm the location of the critical point of the quantum phase transition and to extract the critical exponents.

IV. QUANTUM CRITICALITY OF THE MODEL

We will now study the three-spin model numerically to understand the nature of the phase transition at $h = 1$ and the critical properties. We will use ED to obtain the ground state and low-lying excitations and then compute various thermodynamic quantities like the magnetization and magnetic susceptibility to study the criticality.

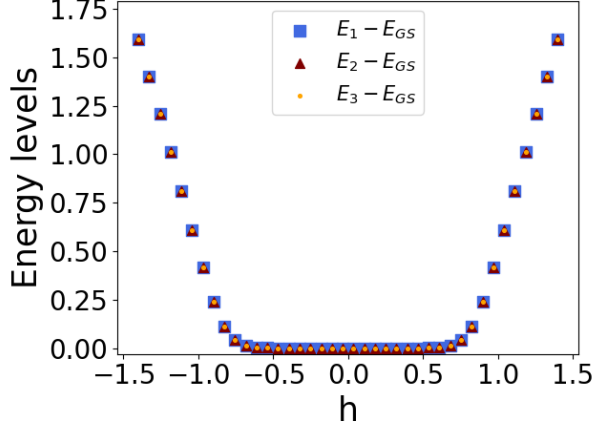


FIG. 2: First three energy levels as measured from the ground state energy plotted as a function of the transverse field h for $L = 15$. We see some degeneracies which arise from the $Z_2 \times Z_2$ symmetry.

A. Energy levels

We use ED to compute the first few energy levels for the Hamiltonian in Eq. (2). The first three excited energy levels with respect to the ground state energy are plotted in Fig. 2. We first notice that the phase transition happens close to $|h| = 1$. In the region $|h| > 1$, the system is gapped with a finite difference between the ground state and the first excited energy. The first three excited states are exactly degenerate due to the symmetries D_1, D_2, D_3 of the model (see Sec. II) with eigenvalues $(D_1, D_2, D_3) = (1, -1, -1), (-1, 1, -1)$ and $(-1, -1, 1)$. The ground state is unique and belongs to the sector $(D_1, D_2, D_3) = (1, 1, 1)$. In the region $|h| < 1$, the ground state becomes degenerate with the three-fold degenerate states as the system size approaches infinity. For finite-sized systems, there is a small gap in the region $|h| < 1$. The gap varies with h and falls off exponentially with the system size; for $h = 0.4$ and $L = 15$, the gap is of the order of 10^{-4} .

B. Finite-size scaling

To understand the nature of the phase transition in this model in comparison to the TFIM which has two-spin interactions, we look at the behaviors of different quantities close to the critical point. Close to the critical point, any singular

quantity, Θ , will have an asymptotic behavior of the form³⁸

$$\Theta \sim |h - h_c|^{-\theta}, \quad (12)$$

where θ is the critical exponent of the quantity Θ . In addition, continuous phase transitions have a diverging correlation length scale ξ which diverges close to the critical point as $\xi \sim |h - h_c|^{-\nu}$, where ν is the critical exponent corresponding to the correlation length. This implies that $\Theta \sim \xi^{\theta/\nu}$. At the critical point, the correlation length diverges. However for finite system sizes, we are limited by the system size L . Hence, when the correlation length exceeds the system size, the quantity will vary with L depending on the ratio L/ξ , and the above relation gets modified to

$$\Theta \sim \xi^{\theta/\nu} \Theta_0(L/\xi), \quad (13)$$

where $\Theta_0(L/\xi)$ is a scaling function with

$$\Theta_0(L/\xi) = \begin{cases} \text{constant} & \text{for } L \gg \xi \\ (L/\xi)^{\theta/\nu} & \text{for } L \ll \xi. \end{cases}$$

Thus at the critical point when $\xi \gg L$, we find that Θ scales as³⁸

$$\Theta|_{h_c} \sim L^{\theta/\nu}. \quad (14)$$

By evaluating Θ for different system sizes we can calculate the critical exponent θ/ν once we know the exact location of the critical point h_c .

C. Numerical determination of critical point

The ground state fidelity is the one of the preliminary ways to detect a quantum phase transition. The fidelity is defined as $\mathcal{F}(h, \delta h) = |\langle \psi_0(h - \delta h/2) | \psi_0(h + \delta h/2) \rangle|$, where $\psi_0(h \pm \delta h/2)$ is the ground state of the Hamiltonian with parameter $h \pm \delta h/2$, and δh is a small but fixed number. The fidelity is expected to show a pronounced deviation from unity in the neighborhood of a phase transition.

In Fig. 3 we show the variation of the fidelity $\mathcal{F}(h, \delta h)$ as a function of the transverse field h for different system sizes $L = 9, 12, 15, 18, 21, 24$ for a fixed $\delta h = 0.005$. We see a dip close to $h = 1$ for all system sizes confirming that a phase transition occurs at this point. As the system size increases, the magnitude of the dip increases and the location of the dip approaches the predicted value $h = 1$. For the largest system size here $L = 24$, we find that the minimum occurs at $h_c = 0.9960$. We also note that the location of the minimum, $h_c(L)$, obtained from the fidelity scales as $h_c(L) = 1 + aL^{-2/\nu}$, while the value of the fidelity susceptibility $\chi_F(h_c = 1) = -\partial^2 \mathcal{F}(h_c, \delta h) / \partial^2 (\delta h) |_{\delta h \rightarrow 0}$ at $h_c = 1$ scales as $bL^{2/\nu}$, where a, b are constants and ν is the correlation length exponent yielding $\nu \approx 0.71$ (see Sec. IV H for further discussion).

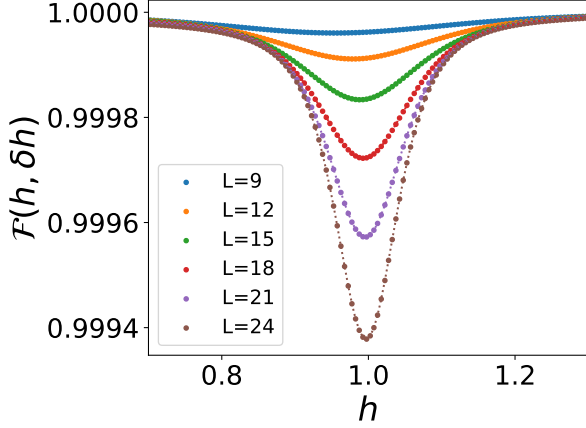


FIG. 3: Fidelity as a function of the transverse field h (for a fixed $\delta h = 0.005$) is plotted for different system sizes $L = 9, 12, 15, 18, 21$ and 24 . There is a dip in the fidelity close to the expected critical point $h = 1$.

D. Dynamical Critical Exponent z

The smallest energy gap in the system at finite sizes (Fig. 2) can be used to estimate the dynamical critical exponent z . As we approach the critical point, the energy difference between the first excited state and the ground state, Δ , behaves as

$$\Delta \sim |h - h_c|^{z\nu}. \quad (15)$$

Given the exponent $z\nu$, Eqs. (12) and (14) imply that

$$\Delta|_{h_c} \sim L^{-z}. \quad (16)$$

We evaluate Δ by performing ED for various system sizes $L = 12, 15, 21, 24$ and 27 in the neighborhood of the critical point. Fig. 4 (a) shows the variation of Δ with h for different system sizes. At $h = h_c$ we plot a log-log graph of $\Delta|_{h_c}$ versus L (inset of Fig. 4 (a)), and fit it linearly to obtain the slope. We find that $z = 1.0267 \pm 0.0014$ indicating that $z = 1$ at criticality.

E. Calculation of central charge c

Since the critical exponent $z = 1$ for this model, the low-lying excitations at the critical point have a linear dispersion making the system Lorentz invariant with some velocity v which will be discussed below. Thus the model can be described by a $1 + 1$ -dimensional conformal field theory char-

acterized by a central charge c ⁶. In such a theory, the von Neumann entanglement entropy of the system can be used to extract the central charge c . If the system is divided into two subsystems A and B, the von Neumann entanglement entropy between the two systems is given by

$$S_A = -\text{Tr}_A(\rho_A \log \rho_A), \quad (17)$$

where ρ_A is the reduced density matrix of the subsystem A obtained by tracing out the states in B from the density matrix of the ground state: $\rho_A = \text{Tr}_B |\psi_{GS}\rangle \langle \psi_{GS}|$. For a finite system size L with PBC, if we divide the system into two subsystems with sizes l and $L-l$, the von Neumann entanglement entropy for the subsystem l is found to be³⁹

$$S(l) = \frac{c}{3} \log[g(l)] + c', \quad (18)$$

where $g(l) = (L/\pi) \sin(\pi l/L)$, and c' is a constant. For our model, we take $L = 27$ and calculate $S(l)$ for different subsystems l , plot $S(l)$ (Fig. 4 (b)) as a function of $\log[g(l)]$, and fit it linearly. The central charge c is three times the slope obtained from this fit which gives $c = 1.0644 \pm 0.0072$.

We can use another method to calculate c . The ground state energy of a finite-sized system is found to show the following dependence on the system size L ³⁹,

$$E_{GS} = \alpha L - \frac{\pi v c}{6L}, \quad (19)$$

where α is a non-universal constant equal to the ground state energy per site in the thermodynamic limit⁴⁰, v is the velocity of the gapless excitations at the critical point which can be obtained from the dispersion, and c is the central charge. We first calculate the velocity by plotting the dispersion for $L = 27$ as shown in the inset of Fig. 4 (c). As discussed earlier, the dispersion varies periodically with the momentum with a period equal to $2\pi/3$. Fitting the inset in Fig. 4 (c) with a function of the form $E = a \sin(bk) + d$, where $a = 2.2893 \pm 0.0134$ and $b = 1.5012 \pm 0.0015$ respectively (the value of b is consistent with a period of $2\pi/3$). Thus the velocity in the linear region near $k = 0$ is $v = ab = 3.4367 \pm 0.0236$. The slope of E_{GS}/L versus $1/L^2$ shown in Fig. 4 (c) gives a slope equal to $-\pi v c/(6L)$. Putting all this together, we get the value of c for this model to be $c = 0.9585 \pm 0.0015$. Thus both the methods give an estimate of c which is close to 1. A value of $c = 1$ suggests the possibility of a marginal operator at the critical point⁴¹ of the three-spin model, and hence weak universality. To investigate this further, we proceed to compute the other critical exponents of this system: β related to the order parameter, γ to the magnetic susceptibility, and ν to the correlation length.

F. Order parameter exponent β

We now study the order parameter in this model. Given the three-spin form of the interaction, we define a symmetric

order parameter as follows. As described earlier, the lattice

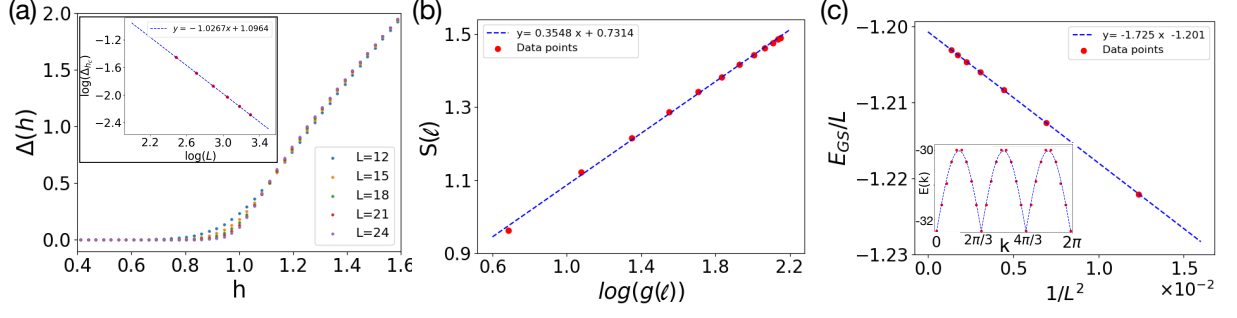


FIG. 4: (a) Plot of the smallest gap, Δ , as a function of h for different system sizes. The inset shows a log-log plot of $\Delta|_{h_c}$ fitting which to a straight line gives the dynamical exponent $z = 1.0267 \pm 0.0014$. (b) Plot of the ground state entanglement entropy versus the logarithm of $g(l) = (L/\pi) \sin(l\pi/L)$, where l is the size of one of the subsystems, and $L = 27$ at the critical coupling $h_c = 1$. The slope of the graph is $c/3$ which gives $c = 1.0644$. (c) From Eq. (19), the variation of the ground state energy with the system size L at $h_c = 1$ gives an estimate for c , namely, the slope of E_{GS}/L versus $1/L^2$ has a slope equal to $-\pi v c / (6L)$. For $L = 27$, we find that $c = 0.9585$. The inset shows the velocity estimate of the gapless excitations which is calculated by fitting the function $E(k) = a \sin(bk) + d$. For $L = 27$, we find $a = 2.2893$ and $b = 1.5012$ respectively giving the velocity $v = ab = 3.4367$.

has three sublattices A, B and C . We define three quantities

$$\begin{aligned} m_A &= \frac{3}{L} \sum_{n=1}^{L/3} \sigma_{3n-2}^z, \\ m_B &= \frac{3}{L} \sum_{n=1}^{L/3} \sigma_{3n-1}^z, \\ m_C &= \frac{3}{L} \sum_{n=1}^{L/3} \sigma_{3n}^z, \end{aligned} \quad (20)$$

and an order parameter

$$m = \sqrt{\langle m_A^2 \rangle + \langle m_B^2 \rangle + \langle m_C^2 \rangle}. \quad (21)$$

For numerical clarity, it would be worthwhile to note here that for finite-size systems, the ground state expectation values $\langle m_a \rangle$ are equal to zero for $a = A, B, C$ even for $h < h_c$. This is due to the fact that the ground state is four-fold degenerate

(in the infinite size limit), and the ground state obtained from ED is a linear combination of these four states making the expectation values exactly equal to zero. To bypass this problem we have first evaluated $\langle m_a^2 \rangle$ and then taken the square root of the squares. The behavior of m for our model as a function of transverse field h is shown in Fig. 5 (a). It begins to drop to zero as we approach h_c . Close to the critical point, we have

$$m \sim |h - h_c|^\beta. \quad (22)$$

From the finite-size scaling of magnetization, we have

$$\mathcal{M}_z \sim L^{\beta/\nu}, \quad (23)$$

where $\mathcal{M}_z = m|_{h_c}$. The log-log graph for \mathcal{M}_z versus L is shown in the inset of Fig. 5 (a); from this we find that $\beta/\nu = 0.1291 \pm 0.0018$. This ratio is close to the value of $\beta/\nu = 1/8$ found for the TFIM (two-spin model) where it is analytically known that $\beta = 1/8 = 0.125$ and $\nu = 1$.

G. Magnetic susceptibility exponent γ

We now compute the magnetic susceptibility χ . For this calculation, we add a longitudinal field to the system so that the Hamiltonian becomes

$$H = - \sum_{j=1}^L [\sigma_j^z \sigma_{j+1}^z \sigma_{j+2}^z + h \sigma_j^x + h_z \sigma_j^z], \quad (24)$$

where h_z is the longitudinal field in the system.

The magnetic susceptibility is defined as⁴²

$$\chi = \frac{\partial \langle M_{h_c} \rangle}{\partial h_z} \Big|_{h_z \rightarrow 0}, \quad (25)$$

where $\langle M_{h_c} \rangle$ is computed as follows. We first define $M = \frac{1}{L} \sum_{i=1}^L \sigma_i^z$ and evaluate its expectation value in the ground state as a function of the transverse and longitudinal fields h_z and h . It will be non-zero due to the presence of the longitudinal field. At the critical point $h_c = 1$ we take the derivative of M_{h_c} with respect to h_z and find its value in the limit $h_z \rightarrow 0$. The magnetic susceptibility as a function of the transverse field h is shown in Fig. 5 (b).

For different system sizes at the critical point we have the quantity $\chi_0 = \chi|_{h_c}$ which, from finite-size scaling, behaves as

$$\chi_0 \sim L^{\gamma/\nu}, \quad (26)$$

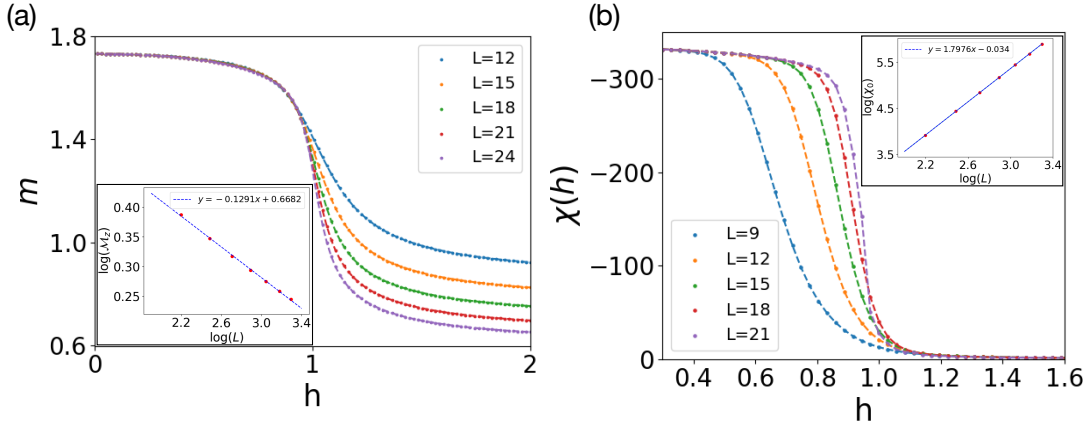


FIG. 5: (a) Plot of the order parameter defined in Eq. (21) versus h for different system sizes. We see that it has a finite value for $h < 1$ and falls off as $h > 1$. The log-log plot of this quantity at the critical point with maximum system size $L = 27$ gives a slope of β/ν close to 0.129. (b) Plot of the magnetic susceptibility for this model as a function of h . At the critical point, it scales with the system size with an exponent γ . From the log-log plot shown in the inset, we find that $\gamma/\nu = 1.7876$.

where γ is the exponent corresponding to susceptibility. This is estimated by plotting a log-log graph of χ_0 versus L as shown in the inset of Fig. 5 (b). The ratio of the exponents γ/ν comes out to be 1.7876 ± 0.0034 for this model, which is again close to the value of $\gamma/\nu = 7/4$ known for the TFIM where $\gamma = 7/4 = 1.75$ and $\nu = 1$.

H. Correlation length exponent ν

To evaluate the correlation length exponent, we return to Eq. (13). Reorganising the equations using the relation, $\tilde{\Theta}(y) = y^\theta \Theta_0(y^\nu)$, we get

$$\Theta \sim L^{\theta/\nu} \tilde{\Theta}(L^{1/\nu} |h - h_c|). \quad (27)$$

For a given singular quantity Θ , by plotting $\Theta(h, L)L^{-\theta/\nu}$ versus $L^{1/\nu}(h - h_c)$ for a range of values of the exponents θ and ν , we find that the data will collapse onto a single curve $\tilde{\Theta}$ when the exponents are closest to their correct values. This finite-size data collapse method can thus be used to determine the critical exponents. In our case, in order to determine ν , we choose three thermodynamic quantities namely the energy gap Δ , the order parameter m and the fidelity susceptibility χ_F . The given thermodynamic quantity Θ times $L^{\theta/\nu}$ is Taylor expanded up to second order as a function of $L^{\tau/\nu}(h - h_c)$ giving the relation

$$\Theta(h, L)L^{\theta/\nu} = a_0 + a_1(L^{\tau/\nu}(h - h_c)) + a_2(L^{\tau/\nu}(h - h_c))^2. \quad (28)$$

where the value of τ is 1 for Δ and m , and is 2 for χ_F ⁴³. The choice of $\tau = 2$ for χ_F requires some explanation. From the

numerical results for χ_F for finite L for the TFIM, we see that while $\chi_F(h_c = 1)$ scales as $L^{2/\nu}$ for the TFIM with $\nu = 1$ as expected, the location of maximum of χ_F does not scale as $h_c(L) - 1 \propto L^{-1/\nu}$ but instead as $h_c(L) - 1 \propto L^{-2/\nu}$. This latter scaling is also consistent with exact results for the fidelity susceptibility for the TFIM⁴⁴. The numerical results for χ_F for the three-spin model indicates exactly the same trend where both the peak height and the deviation of the peak location of χ_F from $h_c = 1$ scales as $L^{2/\nu}$ and $L^{-2/\nu}$ respectively with $\nu \approx 0.71$. We believe that this unusual scaling of the peak location, which forces us to use $\tau = 2$ instead of 1 in Eq. (28) for the scaling collapse of χ_F , is related to the self-dual nature of the critical points in both the models.

We then fit our data to this function in Eq. (28) and extract the values of a_0, a_1, a_2 and ν by minimizing χ^2 for the fit. Furthermore, we take $h_c = 1$, θ/ν is fixed to $z = 1$ for Δ and $\beta/\nu = 1/8$ for m to reduce the number of fitting parameters and equals $2/\nu$ for χ_F . As shown in Fig. 6, we find the estimated values of ν to be 0.82, 0.826 and 0.709 from the data collapse of Δ , m and χ_F respectively. Among the three panels, we see that the data collapse is best for the energy gap Δ (Fig. 6 (a)) where the data for all the system sizes fall very close on top of each other with the available system sizes from ED. However the scaling collapse is not good for the order parameter and fidelity susceptibility and the systematic deviations in Fig. 6 (b), (c) indicate much stronger finite-size corrections in these quantities compared to Δ . Thus we choose the value of $\nu \approx 0.82$ based on the data collapse data of the energy gap Δ for the three-spin model. From this analysis, we see that the critical point of the three-spin model is different from the TFIM (where $\nu = 1$) even though the values of β/ν and γ/ν seem identical.

I. Binder cumulant

Another quantity that shows that the critical behaviour of the three-spin model is different to that of the TFIM is the

Binder cumulant which is defined as^{45–47}

$$U_2 = C + D \frac{\langle m^4 \rangle}{\langle m^2 \rangle^2}, \quad (29)$$

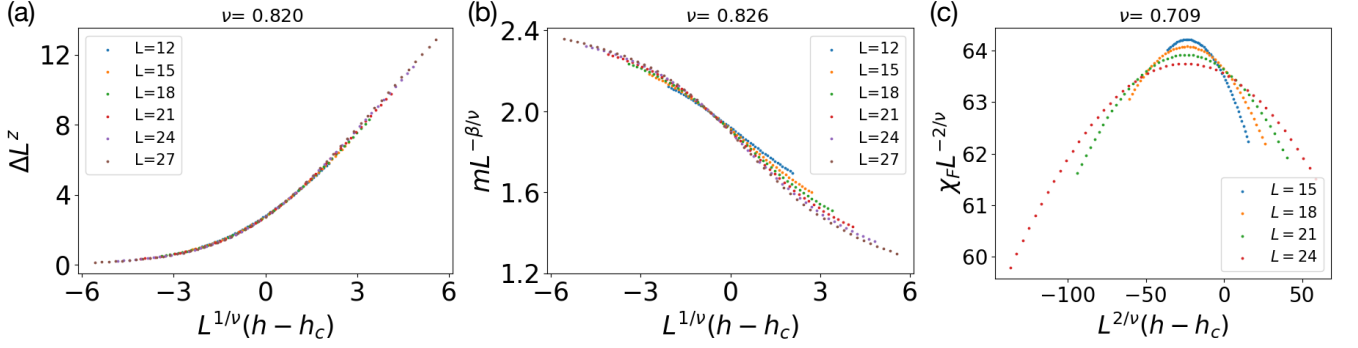


FIG. 6: (a) The scaling collapse of the data from energy gap with ΔL^z versus $L^{1/\nu}(h - h_c)$ is shown for different system sizes. We see that this quantity gives a good data collapse with the plots of different system sizes falling on top of each other for the estimated value of $\nu = 0.82$ obtained by fitting the function in Eq. (28). (b) The scaling collapse using the data of order parameter for different system sizes is shown here. We plot $mL^{-\beta/\nu}$ versus $L^{1/\nu}(h - h_c)$ and obtain the best fit for the polynomial function given with $\nu = 0.826$. (c) The scaling collapse for fidelity susceptibility has a scaling relation $\chi_F^{2/\nu} = f(L^{2/\nu}(h - h_c))$ and the data gives the best estimate of ν to be 0.709.

where the order parameter m and the normalization constants C, D are defined appropriately for a given model so that U_2 has the values 0 and 1 in the thermodynamic limit in the disordered and the ordered phase respectively. For the two-spin TFIM we have $m^2 = (\frac{1}{L} \sum_i^L \sigma_i^z)^2$ with $C = 3/2$ and $D = -1/2$. For our three spin model the order parameter is defined as in the Eq. (21) with $C = 5/2$ and $D = -3/2$ ⁴⁸. Furthermore, $\langle O \rangle$ in Eq. (29) denotes $\langle \psi_0 | O | \psi_0 \rangle$ where $|\psi_0\rangle$ equals the ground state at a finite size L and O equals either m^2 or m^4 . We plot the Binder cumulant for the ground state of H_3 in Fig. 7 as a function of the transverse field h . As expected they cross close to the critical point for different system sizes. More interestingly, for our model, there is a negative dip in U_2 close to the critical point for $L \geq 18$. The dip increases in magnitude as we go to larger system sizes, however it does not increase faster than L ; thus the phase transition close to h_c is still continuous in nature⁴⁹⁻⁵¹. However this is starkly different from the monotonic behavior of U_2 for the two-spin case as can be seen in the inset of Fig. 7.

J. Comparison with transverse field Ising model, hyperscaling, and quantum Ashkin-Teller model

We have repeated the numerical analysis for the TFIM (two-spin Ising model) using ED for system sizes $L = 8, 10, 12, 14, 16, 18, 20$ and 22. In that case our calculations give $z = 1.0026$, $c \approx 0.50$, $\beta/\nu = 0.1337$ and $\gamma/\nu = 1.7936$. It is useful to note that the fidelity susceptibility for the TFIM does not yield a good scaling collapse while the smallest energy gap, Δ , leads to the best scaling collapse near the critical point, just like the three-spin model. For the three-spin model we found above that $z = 1.02$, $\beta/\nu = 0.129$ and $\gamma/\nu = 1.789$ with the data from system sizes $L = 9, 12, 15, 18, 21, 24, 27$. We can see that the values of the ratios of critical exponents β/ν and γ/ν are very close to each other for the two models. However the correlation length critical exponent ν is 1 for the two-spin model (TFIM) and close to 0.8 for the three-

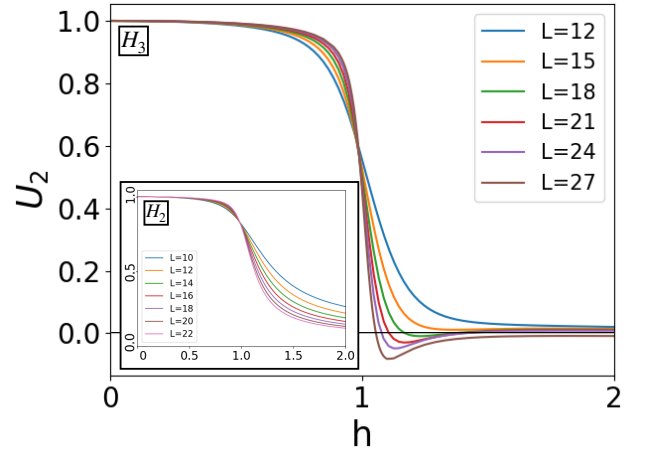


FIG. 7: Plot of Binder cumulant U_2 defined in Eq. (29) as a function of the field h for the three-spin model. The plots for different system sizes cross each other close to h_c . We observe a negative dip close to h_c , the magnitude of which increases with the system size. This is in contrast to the TFIM where the Binder cumulant is a monotonic function as shown in the inset.

spin model. Since all the exponents and the central charge value conform with the theoretical values from analytical and numerical calculations for the two-spin Ising model^{38,52}, we expect that the exponents obtained by the same methods for the three-spin model are also reliable. The estimated values for the two models are tabulated and compared in Table I. Furthermore, we check for the validity of the hyper-scaling relation for our model. The hyperscaling relation is given by³⁸

$$2\beta + \gamma = \nu(d + z), \quad (30)$$

where d is the space dimensionality of the system ($d = 1$ in our case). Since $d, z, \beta/\nu$ and γ/ν are the same for the two-spin and three-spin models, our model also satisfies the hyperscaling relation.

Exponent	Method used	Three-spin	Two-spin
z	Δ scaling with L at h_c	1.0267 (14)	1.0026 (3)
β	m scaling with L at h_c	0.1018 (23)	0.1337 (64)
γ	χ scaling with L at h_c	1.4102 (43)	1.7936 (20)
ν	Data Collapse (m)	0.8261 (189)	1.0019 (62)
	Data Collapse (Δ)	0.8202 (55)	1.0609 (14)
	Data Collapse (χ_F)	0.7092 (4)	0.9604 (6)
c	EE Scaling at h_c	1.0644 (72)	0.5096 (13)
	Energy scaling at h_c	0.9585 (15)	0.5034 (68)

TABLE I: Numerical estimates of the critical exponents and the central charge for the three-spin and two-spin Ising models in a transverse field. Here EE stands for entanglement entropy. The error bars shown are obtained from the fitting procedures as discussed in the text.

Since the central charge $c = 1$ for the three-spin model and the ratios of the critical exponents β/ν and γ/ν are essentially identical to those of the TFIM, this strongly suggests that the critical behavior of the three-spin model belongs to the class of $1 + 1$ -dimensional models with $z = 1$ and $c = 1$ described by the AT model⁵³. The AT model constructed on a lattice has two spin $s = 1/2$ freedom on each site denoted by σ and τ . These operators are coupled by a parameter λ . The Hamiltonian for the quantum AT model is given by⁵⁴

$$H_{AT} = -h \sum_{j=1}^L (\sigma_j^x + \tau_j^x + \lambda \sigma_j^x \tau_j^x) - \sum_{j=1}^L (\sigma_j^z \sigma_{j+1}^z + \tau_j^z \tau_{j+1}^z + \lambda \sigma_j^z \sigma_{j+1}^z \tau_j^z \tau_{j+1}^z). \quad (31)$$

This model is known to exhibit weak universality, namely, the ratios of the exponents $\beta/\nu = 1/8$ and $\gamma/\nu = 7/4$ are independent of λ but the values of the exponents individually depend on λ . One limit of $\lambda = 0$ reduces the AT model to two decoupled TFIM thus giving $c = 1$. For this case we know that $\nu = 1$. In the other limit of $\lambda = 1$, we get the four-state Potts model⁵⁵, with the critical exponent $\nu = 2/3$. We thus see that our three-spin model H_3 also shows this weak universality since $c = 1$, and β/ν and γ/ν are very close to $1/8$ and $7/4$. However ν is different from the TFIM. Since the value of $\nu = 0.82$ for the three-spin model, it must lie somewhere in between two copies of the the TFIM and the four-state Potts model. To find the value of λ for which the three-spin model would get mapped to the AT model, we would have to study the AT model as a function of λ . However since the number of degrees of freedom are doubled, we can go only up to system sizes $L = 13$ using ED, and thus cannot rely on those numerical results. An analytical study using real-space renormalization group gives a relation between the critical exponents ν

and λ as⁵⁶

$$\nu = \frac{1}{2 - (\frac{\pi}{2}) [\arccos(-\lambda)]^{-1}}. \quad (32)$$

Substituting $\nu = 0.82$ gives an effective value of $\lambda = 0.43$ for the critical point of the three-spin model. We would have to perform numerical calculations using the density-matrix renormalization group or quantum Monte Carlo methods to numerically establish the value of λ more precisely. This would be an interesting problem for future studies.

V. PRESENCE OF QUANTUM MANY-BODY SCARS

A. Non-integrability of the model

We now show that the three-spin model is different from the TFIM in that while the latter model is well-known to be integrable, the former seems to be non-integrable. A common diagnostic to test integrability is to study the energy level spacing statistics. In this section, we will study that level spacing for H_3 and discover that shows that the model is non-integrable. If the spectrum of energies is sorted in increasing order so that E_n is the n -th energy level, then we define the level spacing as^{57,58}

$$s_n = E_{n+1} - E_n. \quad (33)$$

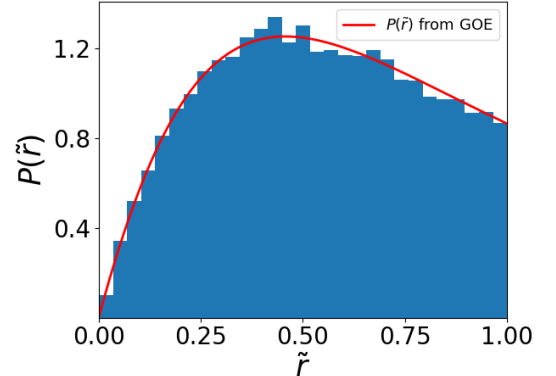


FIG. 8: The distribution of \tilde{r} defined in Eq. (34) is plotted for system size $L = 18$ with open boundary conditions in the sector $(D_1, D_2, D_3) = (1, -1, -1)$ that contains 65536 eigenstates. Further the expected distribution derived for a GOE $P(\tilde{r})$ is shown in red. We see that they agree quite well. The average of \tilde{r} also turns out to be close to 0.53 as expected for GOE.

The distribution of s , called $P(s)$, gives a way of testing the integrability of the system. The system is integrable if $P(s)$ is Poisson-like and is non-integrable if $P(s)$ has a Wigner-Dyson distribution. However, for many-body systems with a non-constant density of states, a new quantity proposed by Oganesyan and Huse⁵⁹ is more useful and reliable. This quan-

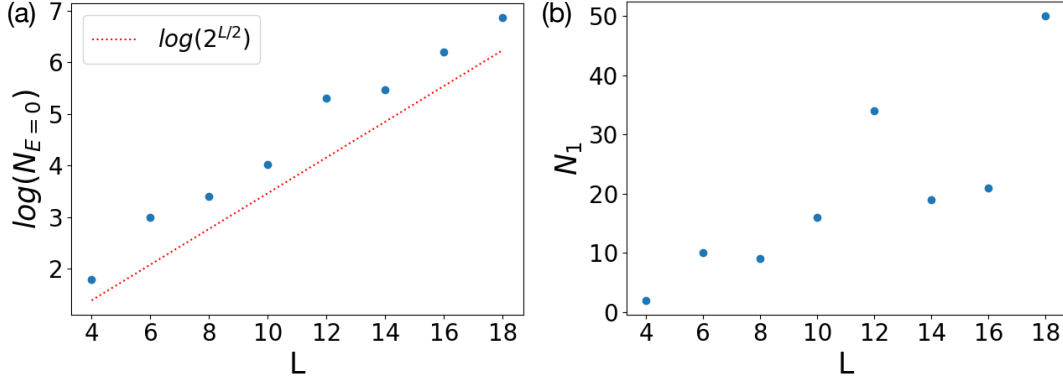


FIG. 9: (a) Plot of logarithm of total number of zero-energy states $N_{E=0}$ versus the system size L . For all L , we see that it is greater than $2^{L/2}$ which is a bound given by an index theorem. (b) Plot of the total number N_1 of Type-I states versus L . This number also generally increases with system size although not monotonically.

tity \tilde{r} is defined as follows

$$\tilde{r} = \frac{\min(s_n, s_{n-1})}{\max(s_n, s_{n-1})}. \quad (34)$$

Since \tilde{r} involves the ratio of energy spacings, the advantage of evaluating \tilde{r} is that it is independent of the local density of states. The definition in Eq. (34) implies that it is restricted to lie in the range 0 to 1. The average value of \tilde{r} turns out to be 0.34 for integrable models but close to 0.53 for non-integrable models governed by the Wigner-Dyson Gaussian orthogonal ensemble (GOE). For our model, we evaluate \tilde{r} in a particular sector $(D_1, D_2, D_3) = (1, -1, -1)$ and with open boundary conditions to eliminate degeneracies due to any residual global symmetries. For $L = 18$, we obtain the value of the

average of \tilde{r} to be 0.533. We further see that the numerical data fits very well to the Wigner-Dyson distribution of $P(\tilde{r})$ given by⁵⁸

$$P(\tilde{r}) = \frac{27}{4} \frac{r + r^2}{(1 + r + r^2)^{5/2}} \Theta(1 - r), \quad (35)$$

where $r_n = s_n/s_{n-1}$ and $\Theta(x)$ is the usual theta function. In Fig. 8, we see that the distribution given in Eq. (35) matches very well with the numerical data. This establishes that the three-spin model is non-integrable. Given that it is non-integrable, we find some of the energy eigenstates with zero energy have an interesting feature as will be discussed in the section below.

B. Zero-energy states

An the interesting property of the three-spin model is that for even system sizes with PBC, we find a large number of states with $E = 0$. These are mid-spectrum states since we have a $E \rightarrow -E$ symmetry of the energy levels. We find that the number of zero-energy increases with system size at least as fast as $2^{L/2}$. We can prove this using an index theorem¹⁵. Writing the Hamiltonian H_3 in the σ^y basis we find that it can be made to have only off-diagonal blocks when the states are divided into two sectors as follows. The spin states for a system size of L is divided into sectors of (i) states with the number of spin states with $\sigma^y = +1$ being even, labeled as $N_{\uparrow, \text{even}}$ (ii) states with the number of spin states with $\sigma^y = +1$ being odd labeled as $N_{\uparrow, \text{odd}}$. This is because for states in $N_{\uparrow, \text{even}}$, the first term in H_3 will flip spins on three sites in the state and the second term will flip one spin, both giving a state with an odd number of up spins, thus connecting to the sector of $N_{\uparrow, \text{odd}}$. The index theorem states that the number of zero-energy states in the system is equal to or greater than

the absolute value of the difference in the number of states in each sector, thus giving a lower bound on the number of zero-energy states. In this case, however, we find that $|N_{\uparrow, \text{even}} - N_{\uparrow, \text{odd}}| = 0$. However we see that the parity operator can be used to further divide these two sectors into states with $P = \pm 1$. Since L is even, we define parity as reflection about the middle of the $(\frac{L}{2})$ -th and $(\frac{L}{2} + 1)$ -th sites and find the number of states with parity $P = \pm 1$ in the two sectors $N_{\uparrow, \text{even}}$ and $N_{\uparrow, \text{odd}}$. Let n_1 be the number of states with $(P = 1, N_{\uparrow, \text{even}})$, n_2 with $(P = 1, N_{\uparrow, \text{odd}})$, n_3 with $(P = -1, N_{\uparrow, \text{even}})$, and n_4 with $(P = -1, N_{\uparrow, \text{odd}})$. We know the following relations between n_1, n_2, n_3 and n_4 .

$$\begin{aligned} n_1 + n_2 + n_3 + n_4 &= 2^L, \\ n_1 + n_3 &= n_2 + n_4 = 2^{L-1}. \end{aligned} \quad (36)$$

Next, given the spin configuration in one of the states, we can see that there are two possibilities. For the system size with L sites, we can have the configuration from site numbers 1 to $L/2$ to be either (i) different from or (ii) same as the configuration from sites L to $(L/2) + 1$. Examples of this

for $L = 6$ are as follows. For the first type, an example of such a configuration is a state like $|\psi\rangle = |\uparrow\uparrow\downarrow\uparrow\downarrow\uparrow\rangle$ for which we see that the spins from 1 to 3 are not the same as from 6 to 4. For such states we can take superpositions $|\psi\rangle + P|\psi\rangle$ and $|\psi\rangle - P|\psi\rangle$ which are eigenstates of P with eigenvalues $+1$ and -1 respectively. These two come in equal numbers for all $|\psi\rangle$. An example of the second type of configuration is $|\uparrow\uparrow\downarrow\downarrow\uparrow\uparrow\rangle$ where the reflection about the midpoint has the same configuration on either side. Such states therefore are eigenvectors of the parity operator with eigenvalue $+1$, i.e. $P|\psi\rangle = \psi$. We also note that such states have to belong to the sector $N_{\uparrow,\text{even}}$ since the total number of up-pointing spins is always twice the number of them till half the lattice. From this, we can conclude that the total number of such states of second type are equal to the difference between the number of $N_{\uparrow,\text{even}}$ with $P = 1$ and $P = -1$. It is also equal to the number of ways of selecting the configuration from sites 1 to $L/2$, since the other half is then fixed by mirror reflection. This gives $2^{L/2}$, which leads to the relation

$$n_1 - n_3 = 2^{L/2}. \quad (37)$$

Turning to the sector $N_{\uparrow,\text{odd}}$, we see that no state can have $P|\psi\rangle = \pm|\psi\rangle$. The combination $|\psi\rangle + P|\psi\rangle$ and $|\psi\rangle - P|\psi\rangle$ again gives equal number of states with eigenvalues ± 1 . This further implies that

$$n_2 = n_4. \quad (38)$$

From Eqs. (36), (37) and (38), we have the following expressions for the numbers of states in the four sectors,

$$\begin{aligned} n_1 &= \frac{1}{2}(2^{L-1} + 2^{L/2}), \\ n_2 &= \frac{1}{2}2^{L-1}, \\ n_3 &= \frac{1}{2}(2^{L-1} - 2^{L/2}), \\ n_4 &= \frac{1}{2}2^{L-1}. \end{aligned} \quad (39)$$

Thus considering the parity sector $P = +1$, we see that a lower bound for the number of zero-energy states is given by $|n_1 - n_2| = \frac{1}{2}2^{L/2}$, and similarly for $P = -1$, we have $|n_3 - n_4| = \frac{1}{2}2^{L/2}$. Adding these up we see that the total number of zero-energy states for this system must satisfy $N_{E=0} \geq 2^{L/2}$. We plot the total number of zero-energy states as a function of L in Fig. 9 (a). We indeed see that the number is greater than the lower bound of $2^{L/2}$ for all values of L .

C. Type-I and Type-II zero modes

We now notice something more interesting about the zero-energy states described in Sec. V B. We again consider the Hamiltonian written in the form given in Eq. (8). It then turns out that the zero-energy states come in two types, Type-I and Type-II. A given zero-energy state $|\psi\rangle$ is said to be Type-II

if $H_3|\psi\rangle = 0$ but the two terms separately do not give zero, i.e., $Z|\psi\rangle \neq 0$ and $X|\psi\rangle \neq 0$. However for a few of the zero-energy states, it turns out that the terms individually also give zero eigenvalues, that is, $Z|\psi\rangle = 0$ and $X|\psi\rangle = 0$. This means that the wave functions of these states are independent of the transverse field h . These Type-I zero modes violate the ETH since they remain unchanged as the coupling h is varied in spite of the energy level spacing in their neighborhood being exponentially small in L ¹⁸ and can, therefore, be classified as quantum many-body scars²³. The number of these Type-I zero-energy states N_1 also increases with system size as shown in Fig. 9 (b). We do not know precisely how fast N_1 grows with the system size L , but we will show below that the growth is at least linear. The speciality of the Type-I states becomes more clear when we look at a plot of the half-chain entanglement entropy versus the energy spectrum of this model. We find that most of the states lie close to the thermal entropy of the system except for some states which stand out at $E = 0$. These are the Type-I zero-energy states which turn out to typically have very low entanglement entropy compared to a generic state close to $E = 0$ showing a violation of the ETH^{60,61}. For a given system size, we can further perform a minimization of the entanglement entropy within the subspace of these scar states²⁰ using the algorithm outlined in Ref. 62. We show these plots with the full spectrum along with the entanglement-entropy minimized scar states in Fig. 10 (a) and (b), for system sizes $L = 12$ and $L = 18$. We see that there is a dramatic drop in the entropy for most of these scar states confirming that they indeed violate the ETH.

System size L	Total number of zero-energy states	Number of Type-I states
4	6	2
6	20	10
8	30	9
10	56	16
12	202	34
14	236	19
16	492	21
18	970	50

TABLE II: Total number of zero-energy states and number of Type-I zero-energy states for various system sizes.

The total number of zero-energy states and the number of Type-I zero-energy states for various system sizes L are shown in Table II. We see that the total number of zero-energy states increases rapidly with L while the number of Type-I states changes non-monotonically but on the average increases with L .

We can further appreciate the difference between Type-II and Type-I states by studying their distribution over the Fock

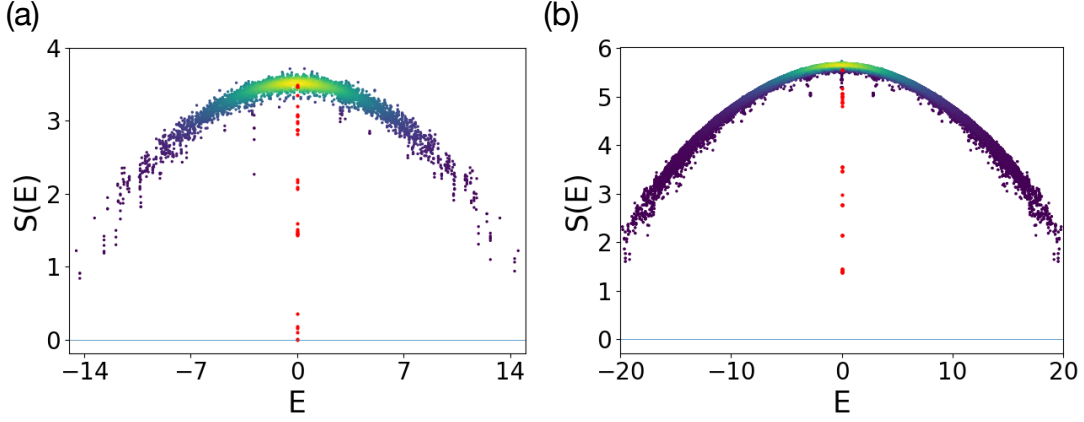


FIG. 10: Plots of the half-chain entanglement entropy spectrum for all the energy levels of the system for $L = 12$ and $L = 18$ are shown in (a) and (b) respectively. The plot in red correspond to the Type-I scar states which have entanglement entropy much lower than the neighbouring states, clearly violating the ETH.

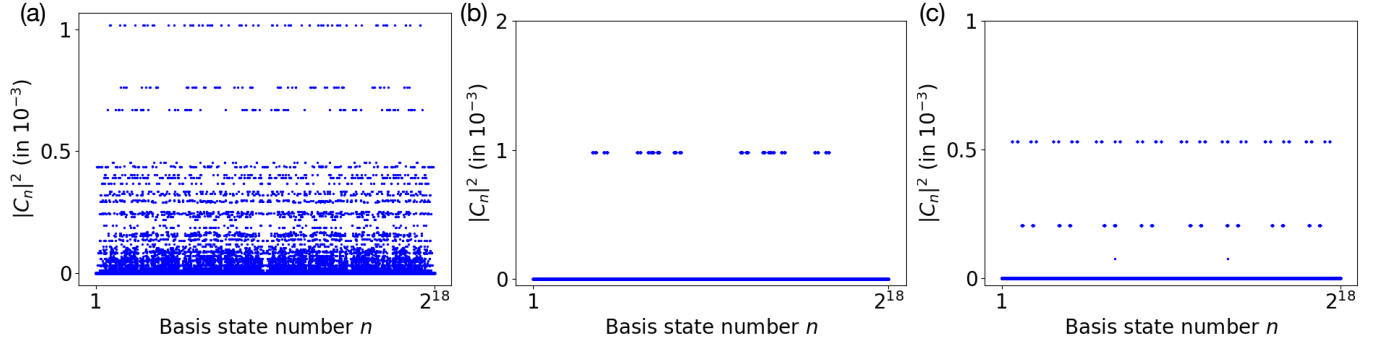


FIG. 11: (a) Probabilities $|c_n|^2$ of a generic Type-II $E = 0$ state in the entire Fock space for all the basis states are plotted for $L = 18$. We see that the distribution is random. (b) and (c) show the same plot for different Type-I scar states. The distribution is more sparse and also has equal probabilities for many basis states.

space. A state can be written as a superposition of the basis states of the entire Fock space. A particular scar state, after it has been minimized for entanglement entropy, can be written as $|\psi_S\rangle = \sum_n c_n |\psi_n\rangle$, where $|\psi_n\rangle$ are the basis states in the Fock space and c_n is the corresponding amplitude for the scar state $|\psi_S\rangle$. In Fig. 11, we plot the probability $|c_n|^2$ for a generic zero-energy state and for the scar states. We see that a Type-II state (Fig. 11 (a)) has non-zero coefficients over a large number of basis states, and the distribution looks random. However, Type-I states as shown in Figs. 11 (b) and (c) can be easily distinguished as they have a large weight over only a few basis states with equal probabilities.

D. Some exact Type-I states

We will now present some Type-I states (scars) which we have found analytically⁶³. To this end, let us define two states

An interesting feature of the Type-I states is that since they are annihilated simultaneously by the operators X and Z and are therefore zero energy eigenstates of the Hamiltonian H_3 for any value of h , they will not evolve with time even if h varies with time in an arbitrary way. In particular, if h is taken to vary periodically with a time period T , the Type-I states will be eigenstates of the Floquet operator U_T which evolves the system over one time period, and the eigenvalue will be exactly equal to 1. While examples of quantum many-body scars has been found in driven systems for specific driving protocols^{65–70}, these Type-I states provide examples of scars for any driving protocol $h(t)$.

involving sites j and k given by

$$\begin{aligned} S_{j,k} &= \frac{1}{\sqrt{2}} (|\uparrow_j \downarrow_k\rangle - |\downarrow_j \uparrow_k\rangle), \\ T_{j,k} &= \frac{1}{\sqrt{2}} (|\uparrow_j \downarrow_k\rangle + |\downarrow_j \uparrow_k\rangle), \end{aligned} \quad (40)$$

where \uparrow and \downarrow denote spin-up and spin-down in the σ^x basis. These are, respectively, spin-singlet and spin-triplet states with total $S^x = (\sigma_j^x + \sigma_k^x)/2 = 0$. Note that these states are antisymmetric and symmetric respectively under the exchange of sites j and k . We find that they satisfy the identities

$$\begin{aligned} \sigma_j^z S_{j,k} &= -\sigma_k^z S_{j,k}, & \sigma_j^z \sigma_k^z S_{j,k} &= -S_{j,k}, \\ \sigma_j^z T_{j,k} &= \sigma_k^z T_{j,k}, & \sigma_j^z \sigma_k^z T_{j,k} &= T_{j,k}. \end{aligned} \quad (41)$$

We now consider a system with L sites with PBC and a state which is a product of singlets with the form

$$|\psi_1\rangle = S_{L,1} S_{L-1,2} S_{L-2,3} \cdots S_{(L/2)+1,L/2}. \quad (42)$$

Clearly $X|\psi\rangle = 0$ where the operator X is given in Eq. (8). (A picture of $|\psi_1\rangle$ for $L = 8$ is shown in Fig. 12 (a)). Each line connecting a pair of sites denotes a spin-singlet state). Eqs. (41) then imply that

$$\begin{aligned} (\sigma_{L-1}^z \sigma_L^z \sigma_1^z + \sigma_L^z \sigma_1^z \sigma_2^z) |\psi_1\rangle &= 0, \\ (\sigma_{L-2}^z \sigma_{L-1}^z \sigma_L^z + \sigma_1^z \sigma_2^z \sigma_3^z) |\psi_1\rangle &= 0, \\ (\sigma_{L-3}^z \sigma_{L-2}^z \sigma_{L-1}^z + \sigma_2^z \sigma_3^z \sigma_4^z) |\psi_1\rangle &= 0, \\ &\vdots \\ (\sigma_{L/2+1}^z \sigma_{L/2+2}^z \sigma_{L/2+3}^z + \sigma_{L/2-2}^z \sigma_{L/2-1}^z \sigma_{L/2}^z) |\psi_1\rangle &= 0, \\ (\sigma_{L/2}^z \sigma_{L/2+1}^z \sigma_{L/2+2}^z + \sigma_{L/2-1}^z \sigma_{L/2}^z \sigma_{L/2+1}^x) |\psi_1\rangle &= 0. \end{aligned} \quad (43)$$

Hence the state $|\psi\rangle$ satisfies $Z|\psi\rangle = 0$ where the operator Z is given in Eq. (8). Since both X and Z annihilate $|\psi\rangle$, we conclude that this is a Type-I state.

Next, we can take the state $|\psi_1\rangle$ and rotate all the sites clockwise by 1 site on the circle. This gives the state

$$|\psi_2\rangle = S_{1,2} S_{L,3} S_{L-1,4} \cdots S_{(L/2)+2,(L/2)+1}, \quad (44)$$

and following similar arguments we can show that $|\psi_2\rangle$ is also a Type-I state. Continuing in this way, we find $L/2$ distinct states, denoted $|\psi_n\rangle$, $n = 1, 2, \dots, L/2$, which are all Type-I states.

Now we observe that if the system is cut into two equal parts by a line, and we consider the state $|\psi_1\rangle$, the line may cut no singlets, one singlet, two singlets, and so on all the way up to $L/2$ singlets, depending on the orientation of the line (see the two dashed lines in Fig. 12 (a)). As a result, the half-chain entanglement entropy can take all possible values from zero up to $(L/2) \ln 2$. Even the largest of these values is only half of the thermal entropy given by $L \ln 2$. This again confirms that these are all scar states.

It turns out that there are two other singlet states, denoted $|\phi_1\rangle$ and $|\phi_2\rangle$, which are also Type-I states. These have the form

$$\begin{aligned} |\phi_1\rangle &= S_{1,2} S_{3,4} S_{5,6} \cdots S_{L-1,L}, \\ |\phi_2\rangle &= S_{2,3} S_{4,5} S_{6,7} \cdots S_{L,1}. \end{aligned} \quad (45)$$

(A picture of $|\phi_1\rangle$ is shown in Fig. 12 (b)). Using Eqs. (41) we can show that these states are also annihilated by the operator

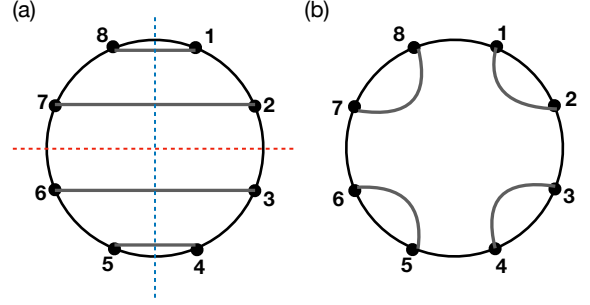


FIG. 12: (a) Picture of the state $|\psi_1\rangle$ given in Eq. (42) for $L = 8$. The lines joining pairs of sites denote spin singlets. Two straight lines dividing the system into two equal parts are shown by dashed lines. The vertical dashed line cuts $L/2$ singlets, while the horizontal dashed line does not cut any singlet; thereby producing half-chain entanglement entropies equal to $(L/2) \ln 2$ and zero respectively. (b) Picture of the state $|\phi_1\rangle$ given in Eq. (45).

Z . (As before, we can find pairs of three-spin terms $\sigma_i^z \sigma_j^z \sigma_k^z$ and $\sigma_l^z \sigma_m^z \sigma_n^z$ such that the sum of the two terms annihilates the states $|\phi_n\rangle$). Further, the half-chain entanglement entropy for these two states range from zero to $2 \ln 2$ depending on the orientation of the line which cuts the system into two halves.

For $L = 4$, the states ψ_n and ϕ_n are identical, and we therefore have only two exact type-I states; according to Table II, these form the complete set of Type-I states. For $L \geq 6$, the states ψ_n and ϕ_n are distinct, and we therefore have $(L/2) + 2$ Type-I states.

The states $|\psi_n\rangle$ and $|\phi_n\rangle$ discussed above are examples of resonating valence bond (RVB) states for a L -site system. If the L sites are arranged around a circle, the RVB states correspond to joining pairs of sites by lines in such a way that no two lines cross each other. According to the Rumer-Pauling rules⁶⁴, there are $L!/(L/2)!((L/2)+1)!$ such states which are linearly independent, although not orthogonal to each other. We see that $(L/2) + 2$ of the RVB states are Type-I states for our model. We conclude that the number of Type-I states increases at least linearly with L .

We can construct one more Type-I state using singlet states as follows. For a system with L sites and PBC, consider the following state which is a product of singlets connecting diametrically opposite sites,

$$|\psi_d\rangle = S_{1,(L/2)+1} S_{2,(L/2)+2} S_{3,(L/2)+3} \cdots S_{L/2,L}. \quad (46)$$

We find that this state is annihilated by terms of the form $\sigma_n^z \sigma_{n+1}^z \sigma_{n+2}^z + \sigma_{(L/2)+n}^z \sigma_{(L/2)+n+1}^z \sigma_{(L/2)+n+2}^z$, where $n = 1, 2, \dots, L/2$. Hence $|\psi_d\rangle$ is annihilated by the operator Z given in Eq. (8). A picture of $|\psi_d\rangle$ for $L = 8$ is shown in Fig. 13 (a). However, $|\psi_d\rangle$ is not an RVB state since the different singlet lines cross each other; in fact, any two singlet lines cross each other. But we can write $|\psi_d\rangle$ as a linear combination of RVB states by using the identity

$$S_{i,j} S_{k,l} - S_{i,k} S_{j,l} + S_{i,l} S_{j,k} = 0 \quad (47)$$

several times. Depending on how four sites labeled i, j, k, l

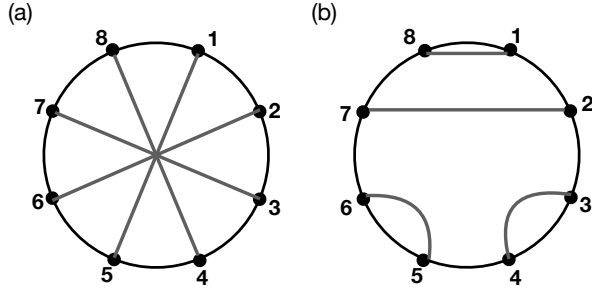


FIG. 13: (a) Picture of the state $|\psi_d\rangle$ given in Eq. (46) for $L = 8$. The lines joining pairs of diametrically opposite sites denote spin singlets. (b) Picture of the state $|\phi_d\rangle$ given in Eq. (48).

are arranged around a circle, one of the terms in Eq. (47) will correspond to a state with one crossing while the other two terms will correspond to non-crossing states. Hence, by repeatedly using Eq. (47), we can successively decrease the number of crossings to eventually reduce $|\psi_d\rangle$ to a superposition of RVB states. For $L = 8$, we find that the superposition contains all the states shown in Figs. 12 (a) and (b) as well as a *specific* linear combination of 8 other RVB states which are of the form

$$|\phi_d\rangle = S_{1,8} S_{2,7} S_{3,4} S_{5,6}, \quad (48)$$

shown in Fig. 13 (b), and 7 other states obtained from Eq. (48) by rotating all the sites clockwise by 1, 2, ..., 7 sites.

The different kinds of exact Type-I states discussed above do not exhaust all the Type-I states. For instance, Table II shows that there are 9 Type-I states for $L = 8$, but the arguments above only account for $(L/2) + 2 + 1 = 7$ of them.

Finally, we note that if L is a multiple of 6, we can find exact Type-I states involving both singlets and triplets. Two such states are shown in Figs. 14 for a system with 6 sites. The state in Fig. 14 (a) has the form

$$|\psi'_1\rangle = T_{6,1} S_{5,2} T_{4,3}, \quad (49)$$

while the state in Fig. 14 (b) has the form

$$|\phi'_1\rangle = T_{1,2} S_{3,4} T_{5,6}. \quad (50)$$

These can be shown to be Type-I states by similar arguments as above and using the identities in Eqs. (41). Then one can repeatedly rotate all the sites by 1 site from $|\psi'_1\rangle$ and $|\phi'_1\rangle$ obtain states of the form $|\psi'_n\rangle$, $n = 1, 2, 3$, and $|\phi'_n\rangle$, $n = 1, 2, \dots, 6$, respectively. We thus obtain 9 states each of which involves one singlet and two triplets. However, one can show that only 5 of these states are linearly independent; one can choose these to be of the form $|\phi'_n\rangle$, where $n = 1, 2, \dots, 5$. For $L = 6$, therefore, we get $(L/2) + 2 = 5$ states involving only singlet states and 5 state involving both singlets and triplets. This gives a total of 10 Type-I states for $L = 6$ which is in agreement with Table II.

A similar construction of Type-I states involving singlets and triplets exists whenever L is a multiple of 6. There are

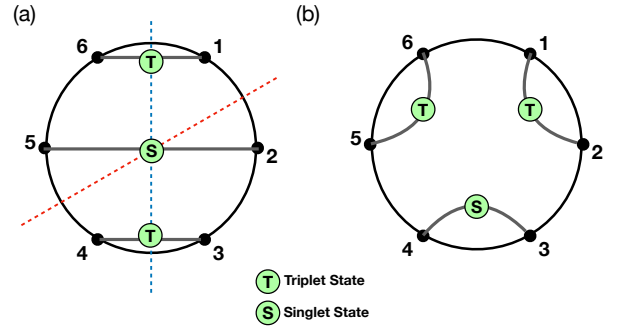


FIG. 14: (a) Picture of the state $|\psi'_1\rangle$ given in Eq. (49) for $L = 6$. The lines joining pairs of sites denote spin singlets or triplets shown as S or T respectively. The dashed lines divide the system into two equal parts and they cut one and three bonds respectively. (b) Picture of the state $|\phi'_1\rangle$ given in Eq. (50).

two kinds of such states. The first kind of states resembles the one shown in Fig. 14 (a) and is given by

$$|\psi'_1\rangle = T_{L,1} S_{L-1,2} T_{L-2,3} T_{L-3,4} \cdots S_{L-4,5} \cdots T_{L/2+3,L/2-2} S_{L/2+2,L/2-1} T_{L/2+1,L/2}, \quad (51)$$

and similar states obtained by rotating all the sites by 1 site. The pattern of bonds from the top to the bottom follows the pattern $TSTTSTT \cdots STTST$. There are $L/2$ states of this kind. The second kind of states resembles the one shown in Fig. 14 (b) and is given by

$$|\phi'_1\rangle = T_{1,2} S_{3,4} T_{5,6} T_{7,8} S_{9,10} T_{11,12} \cdots T_{L-5,L-4} S_{L-3,L-2} T_{L-1,L}, \quad (52)$$

and similar states obtained by rotating all the sites by 1 site. The bonds follow the pattern $TSTTSTT \cdots STTST$ around the circle. There are 6 states of this kind. We therefore have a total of $(L/2) + 6$ Type-I states, each of which is a product of $L/6$ singlets and $L/3$ singlets. However, unlike the Type-I states which involve only singlets where we found that there are $(L/2) + 2$ linearly independent states, we do not know how many of the $(L/2) + 6$ Type-I states involving singlets and triplets are linearly independent for a general value of L . For $L = 6$, we saw above that the number of independent states is 5, but a formula for $L = 12, 18, 24, \dots$ is not known.

Once again, we note that when the system is cut into two equal parts by a line, the number of bonds (singlets or triplets) cut by the line can vary from zero to $L/2$ depending on its orientation (see Fig. 14 (a)). The half-chain entanglement entropy can therefore vary from zero up to $(L/2) \ln 2$ which is much smaller than the thermal entropy equal to $L \ln 2$.

The fact that there are several exact Type-I states involving singlets and triplets which appear only when L is a multiple of 6 may help to explain why there is a jump in the number of Type-I states whenever L hits those particular values, as we can see in Table II.

It would be interesting to find all possible Type-I states ex-

actly but this seems to be a difficult problem. We note that all the exact Type-I states discussed in this section have been found by demanding that they be annihilated by the sum of two three-spin terms of the form $\sigma_i^z \sigma_j^z \sigma_k^z + \sigma_l^z \sigma_m^z \sigma_n^z$, and these sums combine to give the total operator Z in Eq. (8). However, there may be more complicated Type-I states which are only annihilated by the sum of three or more three-spin terms.

It is intriguing that singlets and triplets (with zero magnetization) play such an important role in the construction of Type-I states even though the Hamiltonian H_3 is not invariant under $SU(2)$ or any other continuous symmetry.

VI. ANOMALOUS RELAXATION OF AUTOCORRELATORS AT DIFFERENT SITES

The ordered phase of the TFIM on a semi-infinite system is characterized by a doubly degenerate spectrum and the presence of a strong edge mode operator that connects pairs of degenerate states with opposite parity^{29,30}. Numerically, this can be observed by studying the infinite-temperature autocorrelator of the σ^z operator at different sites near the edge of the system^{31–33}.

$$A_l^{zz}(t) = \frac{1}{2L} \text{Tr}[\sigma_l^z(t) \sigma_l^z]. \quad (53)$$

Since the strong mode operator has a large overlap with the operator σ_1^z operator at the boundary site, the autocorrelator shows a long plateau near the value of unity with a time scale that increases exponentially with the system size before relaxing to zero. However the autocorrelator of σ^z at any other site falls off to zero very quickly in a time scale $t \lesssim 10$.

This motivates us to ask a similar question for the non-integrable model H_3 with open boundary conditions. As discussed earlier, this model has an exact degeneracy in three-fourths of its eigenstates due to the presence of the D_1 , D_2 , D_3 operators for PBC, and also a two-fold degeneracy in half of its eigenstates due to parity symmetry for open boundary conditions. These degeneracies are present for any value of the transverse field h . We will study how the spin autocorrelators relax in time at sites near the boundary for various values of h and see if the degeneracies play any role in the relaxation. The infinite-temperature autocorrelators can be calculated as traces over all the energy eigenstates of the Hamiltonian. We will be interested in the zz - and xx -autocorrelators given by

$$A_l^{zz}(t) = \frac{1}{2L} \sum_{n,m} e^{i(E_n - E_m)t} |\langle n | \sigma_l^z | m \rangle|^2, \quad (54)$$

and

$$A_l^{xx}(t) = \frac{1}{2L} \sum_{n,m} e^{i(E_n - E_m)t} |\langle n | \sigma_l^x | m \rangle|^2, \quad (55)$$

respectively. The autocorrelators defined in this way are expected to reveal the nature of the phase transition and the energy spectra on the two sides of the transition.

We present the results for $A_l^{zz}(t)$ versus t on a log scale for different lattice sites $l = 1, 2, \dots, 6$ (with $l = 1$ being the boundary site) and three values of the transverse field, $h = 0.2, 1$, and 5.0 , in Figs. 15 (a), (b) and (c) respectively. The relaxation of the autocorrelators shows very interesting behaviors depending on whether $h \ll 1$, $h \gg 1$ or $h = 1$. For $h = 0.2$ (see Fig. 15 (a)), we observe qualitatively that A_1^{zz} and A_4^{zz} have a similar structure, with a small plateau for a time interval of $t \lesssim 10^4$, where the autocorrelator remains near 1 before falling off to zero at large times. We believe that this is due to the presence of an operator, which has an appreciable overlap with σ^z at sites 1 and 4 and also has a small commutator with the Hamiltonian itself. The autocorrelator at site $l = 2$ has the most striking behavior, showing oscillations with an approximate period of 15.5. We also plot the same autocorrelator in real time instead of the logarithmic scale in Fig. 16 (a), where the oscillations can be seen clearly.

The small frequency oscillations at the site $l = 2$ can be explained by considering the Hamiltonian in the small h limit and doing a perturbative calculation. First, by putting $h = 0$, we have the Hamiltonian given by $H_3|_{h=0} = Z = -\sum_{j=1}^{L-2} \sigma_j^z \sigma_{j+1}^z \sigma_{j+2}^z$. The eigenstates of this are given by product states where each site j has a definite value of $\sigma_j^z = \pm 1$. Therefore, all the eigenvalues of Z are integer valued and so are the energy differences. Now, an introduction of a small value of transverse field h gives eigenstates with energy differences of order h . To see this, we look at the couplings in the Z term and the effects of σ_l^z in the autocorrelator more carefully. The couplings in Z containing a particular σ_l^z can be considered for three separate cases, (a) $\sigma_l^z(\sigma_2^z \sigma_3^z)$, for $l = 1$, (b) $\sigma_l^z(\sigma_1^z \sigma_3^z + \sigma_3^z \sigma_4^z)$, for $l = 2$, and (c) $\sigma_l^z(\sigma_{l-2}^z \sigma_{l-1}^z + \sigma_{l-1}^z \sigma_{l+1}^z + \sigma_{l+1}^z \sigma_{l+2}^z)$, for $l \geq 3$. Since each σ_j^z can take values ± 1 , the products of two spin operators also will take values ± 1 . Therefore, in cases (a) and (c), we have a sum of an odd number of such products which necessarily has a non-zero value. However, in case (b), we have an even number of such terms and hence, for $l = 2$, we can have a case where σ_2^z is multiplied by zero. More precisely, this happens if $\sigma_3^z(\sigma_1^z + \sigma_4^z) = 0$, i.e., if $(\sigma_1^z + \sigma_4^z) = 0$. Thus, the two sets of eigenstates of Z corresponding to the value of $\sigma_2^z = \pm 1$ (we label them as $|I\rangle$ and $|II\rangle$ respectively) will be degenerate for any values of $\sigma_1^z, \sigma_3^z, \sigma_4^z, \sigma_5^z, \sigma_6^z, \dots$, with the condition that $(\sigma_1^z + \sigma_4^z) = 0$. This condition is satisfied for half of the states when σ_1^z and σ_4^z are opposite to each other, and then we have a pairwise degeneracy between the states of types $|I\rangle$ and $|II\rangle$. With a small h present, the term $-h\sigma_2^x$ will break the degeneracy, since $\sigma_2^x |I\rangle = |II\rangle$ and vice-versa. Therefore we end up having a new set of eigenstates $|\pm\rangle = 1/\sqrt{2}(|I\rangle \pm |II\rangle)$ with an energy splitting of $2h$. Now, since $\langle - | \sigma_2^z | + \rangle = 1$, we see from Eq. (54) that for $l = 2$, half the states of the spectrum in the autocorrelator will contribute to an oscillatory term $e^{\pm i2ht}$. This exactly explains the oscillations seen in Fig. 16 (a). Eventually, for later times the oscillations decay as terms of order h^2 and higher in the energy differences become important.

We also note that since $|\pm\rangle$ are eigenstates of σ_2^x , with eigenvalues ± 1 , these states will contribute to the diagonal

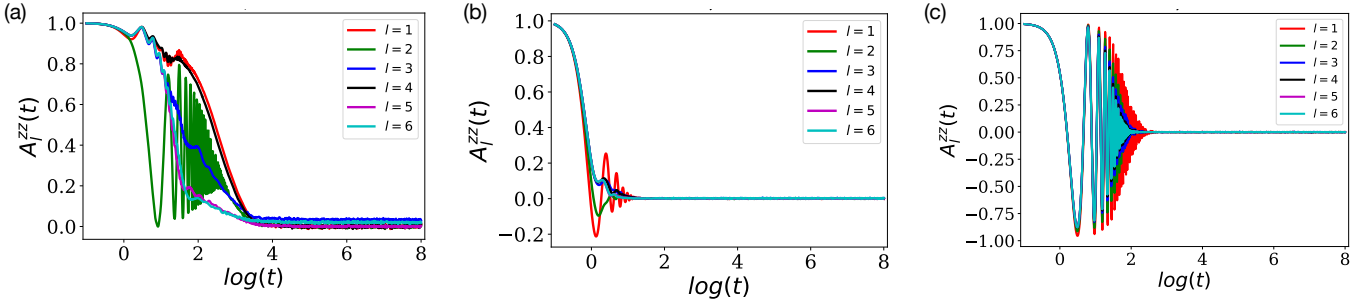


FIG. 15: Autocorrelation function $A_l^{zz}(t)$ for $L = 14$ plotted versus time on a log scale for different values of the transverse field. Deep inside the ordered phase, (a) $h = 0.2$, or the disordered phase, (c) $h = 5$, the autocorrelators at several sites near the boundary show oscillations for a long time before decaying to zero. (b) At the critical point, $h = 1$, the autocorrelators decay quickly to zero at all sites except at the boundary site.

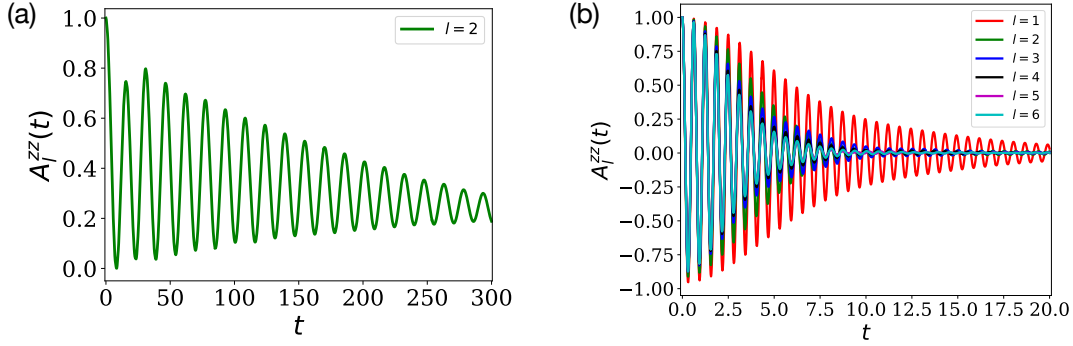


FIG. 16: (a) $A_l^{zz}(t)$ at site $l = 2$ for $h = 0.2$, showing long-time oscillations. This can be understood using first-order degenerate perturbation theory. (b) $A_l^{zz}(t)$ showing oscillations at different sites for $h = 5$. This can be understood using effective two-level systems. Both the figures are for system size $L = 14$.

terms (i.e., terms with $m = n$ and therefore $E_m = E_n$) in the xx -autocorrelator at $l = 2$ in Eq. (55). Since the diagonal terms are time-independent (as $E_m = E_n$), we expect that the xx -autocorrelator at $l = 2$ will have a non-zero constant term. This agrees with what we see in Fig. 18 (a) for $h = 0.2$.

For large values of h , we see in Fig. 16 (b) that at several sites near one end of the system, the zz -autocorrelators show pronounced oscillations before eventually decaying to zero. All the oscillations have the same frequency which is found to be close to $2h$. We can understand this as follows. For $h \gg 1$, we see from Eq. (2) that the eigenstates of H are given, to lowest order, by products of eigenstates of σ_j^x for all j . An operator σ_j^z connects two states which have $\sigma_j^x = \pm 1$ and therefore unperturbed energies equal to $\mp h$. The energy difference of these two states is $2h$, hence Eq. (54) implies that the contribution of these two states to the zz -autocorrelator at site j will oscillate as $e^{\pm i2ht}$; this explains Fig. 16 (b). Next, we can extend this argument to first order in perturbation theory. Consider the zz -autocorrelator at the first site given by $j = 1$ where the oscillations are most pronounced. To first order in the perturbation $V = -\sigma_1^z \sigma_2^z \sigma_2^z$, the two states given by $|I\rangle = |\sigma_1^x = +1, \sigma_2^x = a, \sigma_3^x = b\rangle$ and $|II\rangle = |\sigma_1^x = -1, \sigma_2^x = -a, \sigma_3^x = -b\rangle$ will mix (here a, b can take values ± 1). The unperturbed energies of these states are $E_I = -h(1 + a + b)$ and $E_{II} = h(1 + a + b)$ respectively.

Hence, to first order in perturbation theory, the energy of the state lying close to $|I\rangle$ will shift from $E_I = -h(1 + a + b)$ to $E'_I = -h(1 + a + b) + 1/(E_I - E_{II}) = -h(1 + a + b) - 1/(2h(1 + a + b))$. Similarly, the perturbation V mixes the two states $|III\rangle = |\sigma_1^x = -1, \sigma_2^x = a, \sigma_3^x = b\rangle$ and $|IV\rangle = |\sigma_1^x = 1, \sigma_2^x = -a, \sigma_3^x = -b\rangle$, and shifts the energy of the state lying close to $|III\rangle$ from $E_{III} = h(1 - a - b)$ to $E'_{III} = h(1 - a - b) + 1/(2h(1 - a - b))$. The operator σ_1^z connects the states lying close to $|I\rangle$ and $|III\rangle$, and we see from the expressions above that the energy difference between these two states is

$$\begin{aligned} |E'_I - E'_{III}| &= 2h + \frac{1}{2h} \left(\frac{1}{1 + a + b} + \frac{1}{1 - a - b} \right) \\ &= 2h + \frac{1}{h} \left(\frac{1}{1 - (a + b)^2} \right). \end{aligned} \quad (56)$$

According to Eq. (54), therefore, the oscillations will have the frequency given in Eq. (56). Now, since a, b can independently take the values ± 1 , giving rise to four possibilities, the expression in Eq. (56) can take two possible values given by $2h + (1/h)$ (when $a = -b$) and $2h - (1/3h)$ (when $a = b$). Hence we expect the oscillations to have a frequency ω , where $\omega/(2h) = 1 + 1/(2h^2)$ and $1 - 1/(6h^2)$. Since these two cases appear an equal number of times, the average value is given

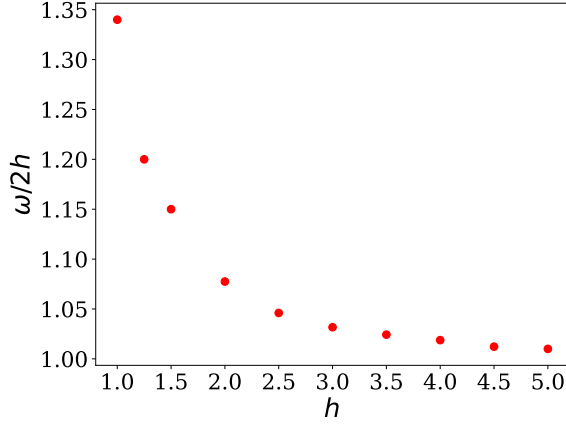


FIG. 17: Variation of the frequency of oscillations of $A_{i=1}^{zz}(t)$ at the end site with the transverse field h for $L = 14$. For large h the dependence is consistent with the perturbative result $\omega/(2h) = 1 + 1/(6h^2)$.

by $\omega/(2h) = 1 + (1/6h^2)$. This is in reasonable agreement with the numerical result shown in Fig. 17 for large values of h . We note that since the frequency ω used in that figure is obtained by calculating the position of the peak of the Fourier transform of the oscillations in Fig. 16 (b), the decay of the oscillations leads to a small width around the peak. This width also turns out to be of the order of $1/h$, and we therefore do not see two separate peaks at $\omega = 2h + (1/h)$ and $2h - (1/3h)$. Remarkably, these early and intermediate time oscillations in $A_i^{zz}(t)$ persist all the way to $h = 1$ (Fig. 17) for the boundary site when the critical point is approached from $h > 1$, while the other autocorrelators show a reasonably rapid decay in the neighborhood of the critical point (see Appendix B for the extraction of the oscillation frequency ω in Fig. 17).

VII. DISCUSSION

A summary of our main results is as follows. Motivated by the one-dimensional TFIM which is one of the best studied integrable models with duality and a quantum critical point, we have made a detailed study of a generalization in which there are Ising interactions between three successive spins (instead of two successive spins as in the TFIM). We find that the model has a $Z_2 \times Z_2$ symmetry for a system with PBC provided that the system size is a multiple of 3. This symmetry implies that the system consists of four sectors which are decoupled from each other, and this leads to three-fold degeneracies in the energy spectrum which involves states from three of the four sectors. Next we have discussed the duality of the model between h and $1/h$. While the duality is straightforward to show for an infinite-sized system, the existence of a duality turns out to be a subtle issue for finite-sized systems with PBC. We find that exact duality holds only if the system size is *not* a multiple of 3. Next, we make a detailed study of the criticality properties of the model at the self-dual point given by $h = 1$. Using ED and system sizes up to $L = 27$,

we use finite-size scaling to first confirm that there is indeed a critical point at $h = 1$, and then to compute the dynamical critical exponent z , the order parameter exponent β , the magnetic susceptibility exponent γ , and the correlation length exponent ν . We find that $z = 1$ suggesting that the low-energy sector of the model at $h = 1$ has conformal invariance. We then determine the central charge c in two different ways (from the length-dependences of the entanglement entropy between two parts of the system and of the ground state energy). We find that c is close to 1. We then observe that although the values of β , γ and ν for the two-spin and three-spin models are different from each other, the ratios β/ν and γ/ν are the same in the two models. This suggests that there is a weak universality and the three-spin model lies on the AT line, just like two copies of the TFIM and the four-state Potts model. All models on this line are known to have $z = 1$, $c = 1$, and the same values of $\beta/\nu = 1/8$ and $\gamma/\nu = 7/4$. There is a quantum AT model which has a parameter λ such that two copies of the TFIM and the four-state Potts model correspond to $\lambda = 0$ and 1 respectively. Given our numerically obtained value of ν for the three-spin model, we estimate this model corresponds approximately to $\lambda \approx 0.43$. A useful direction for future studies would be to determine all these quantities (z , β , γ , ν , c and λ) more accurately for the three-spin model using density-matrix renormalization group or quantum Monte Carlo methods which can be used for much larger system sizes.

We then studied the energy level spacing statistics in a particular symmetry sector of a system with open boundary conditions to determine if the three-spin model is integrable. We find that the level spacing statistics has the form of the Gaussian orthogonal ensemble, and hence the model is non-integrable. Next, we find that the model has an exponentially large number of mid-spectrum zero-energy states which is consistent with an index theorem; the number of states grows at least as fast as $2^{L/2}$. Further, we find that the zero-energy states are of two types which we call Type-I and Type-II. The Type-I states are special because they are simultaneous zero-energy eigenstates of the two parts of the Hamiltonian (the three-spin interaction and the transverse field); hence their wave functions do not change with h in spite of the energy level spacing in their neighborhood being exponentially small in system size. These states thus violate the ETH and qualify as quantum many-body scars. We have presented the analytical forms of some of the Type-I states which show that their number grows at least linearly with the system size. However we do not know the form of the growth more precisely (linear, exponential, or some other dependence). Finally, we have studied the infinite-temperature autocorrelation functions for both σ^x and σ^z at sites close to one end of a large system with open boundary conditions. We find that far from the critical point, at either $h \ll 1$ or $h \gg 1$, some of the autocorrelators show an anomalous behavior in that they show pronounced oscillations and decay very slowly with time. The time scale of decay is much larger than the inverse of the energy scales in the Hamiltonian; this is unexpected since the model is non-integrable. We provide a qualitative understanding of the oscillations using perturbation theory. However, the reason for a large decay time is not yet understood analytically. Further-

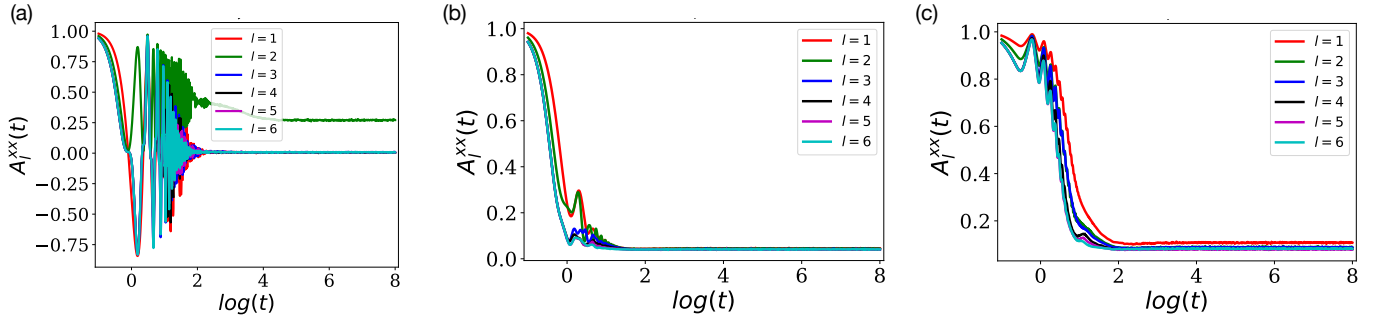


FIG. 18: Autocorrelation function $A_l^{xx}(t)$ for $L = 14$ plotted versus time on a log scale for different values of the transverse field, (a) $h = 0.2$, (b) $h = 1$, and (c) $h = 5$.

more, the autocorrelator for σ^z at the end site shows persistent oscillations at short and intermediate timescales even when h is close to the critical point while the other autocorrelators decay quickly to zero. An analytic understanding of this feature is lacking as of now.

Acknowledgments

A.S. thanks Hosho Katsura for illuminating discussions.

D.S. thanks Chethan Krishnan for stimulating discussions in the early stages of this work. A.S. and D.S. acknowledge useful discussions with the participants in the ICTS program “Periodically and quasi-periodically driven complex systems” (code: ICTS/pdcs2023/6). S.S. thanks MHRD, India for financial support through the PMRF. D.S. acknowledges funding from SERB, India through project JBR/2020/000043.

- ¹ P. Pfeuty, *Annals of Physics* **57**, 79 (1970).
- ² R. B. Stinchcombe, *J. Phys. C* **6**, 2459 (1973).
- ³ S. Sachdev, *Quantum Phase Transitions* (Cambridge University Press, Cambridge, 1999).
- ⁴ H. A. Kramers and G. H. Wannier, *Phys. Rev.* **60**, 252 (1941).
- ⁵ R. Savit, *Rev. Mod. Phys.* **52**, 453 (1980).
- ⁶ P. Francesco, P. Mathieu, and D. Senechal, *Conformal Field Theory* (Springer, 1999).
- ⁷ L. Turban, *J. Phys. C* **15**, L65 (1982).
- ⁸ K. A. Penson, R. Jullien, and P. Pfeuty, *Phys. Rev. B* **26**, 6334 (1982).
- ⁹ A. Maritan, A. Stella, and C. Vanderzande, *Phys. Rev. B* **29**, 519 (1984).
- ¹⁰ F. Iglói, D. V. Kapor, M. Skrinjar, and J. Sólyom, *J. Phys. A* **19**, 1189 (1986).
- ¹¹ M. Kolb and K. A. Penson, *J. Phys. A* **19**, L779 (1986).
- ¹² F. C. Alcaraz and M. N. Barber, *J. Phys. A* **20**, 179 (1987).
- ¹³ J. K. Pachos and M. B. Plenio, *Phys. Rev. Lett.* **93**, 056402 (2004).
- ¹⁴ H. P. Büchler, A. Micheli, and P. Zoller, *Nature Phys.* **3**, 726 (2007).
- ¹⁵ M. Schecter and T. Iadecola, *Phys. Rev. B* **98**, 035139 (2018).
- ¹⁶ C.-J. Lin and O. I. Motrunich, *Phys. Rev. Lett.* **122**, 173401 (2019).
- ¹⁷ C.-J. Lin, V. Calvera, and T. H. Hsieh, *Phys. Rev. B* **101**, 220304(R) (2020).
- ¹⁸ D. Banerjee and A. Sen, *Phys. Rev. Lett.* **126**, 220601 (2021).
- ¹⁹ V. Karle, M. Serbyn, and A. A. Michailidis, *Phys. Rev. Lett.* **127**, 060602 (2021).
- ²⁰ S. Biswas, D. Banerjee, and A. Sen, *SciPost Phys.* **12**, 148 (2022).
- ²¹ H. Bernien, S. Schwartz, A. Keesling, H. Levine, A. Omran, H. Pichler, S. Choi, A. S. Zibrov, M. Endres, M. Greiner, V. Vuletic, and M. D. Lukin, *Nature* **551**, 579 (2017).
- ²² S. Moudgalya, N. Regnault, and B. A. Bernevig, *Phys. Rev. B* **98**, 235156 (2018).
- ²³ C. J. Turner, A. A. Michailidis, D. A. Abanin, M. Serbyn, and Z. Papić, *Nature Phys.* **14**, 745 (2018).
- ²⁴ C. J. Turner, A. A. Michailidis, D. A. Abanin, M. Serbyn, and Z. Papić, *Phys. Rev. B* **98**, 155134 (2018).
- ²⁵ M. Schecter and T. Iadecola, *Phys. Rev. Lett.* **123**, 147201 (2019).
- ²⁶ N. Shibata, N. Yoshioka, and H. Katsura, *Phys. Rev. Lett.* **124**, 180604 (2020).
- ²⁷ G.-X. Su, H. Sun, A. Hudomal, J.-Y. Desaulles, Z.-Y. Zhou, B. Yang, J. C. Halimeh, Z.-S. Yuan, Z. Papić, and J.-W. Pan, *Phys. Rev. Research* **5**, 023010 (2023).
- ²⁸ K. Sanada, Y. Miao, and H. Katsura, *arXiv:2304.13624*.
- ²⁹ P. Fendley, *J. Stat. Mech.* **P11020** (2012).
- ³⁰ P. Fendley, *J. Phys. A* **49**, 30LT01 (2016).
- ³¹ J. Kemp, N. Y. Yao, C. R. Laumann, and P. Fendley, *J. Stat. Mech.* **063105** (2017).
- ³² D. J. Yates, A. G. Abanov, and A. Mitra, *Phys. Rev. Lett.* **124**, 206803 (2020).
- ³³ D. J. Yates, A. G. Abanov, and A. Mitra, *Phys. Rev. B* **102**, 195419 (2020).
- ³⁴ M. Suzuki, *Prog. Theor. Phys.* **51**, 1992 (1974).
- ³⁵ O. F. de Alcantara Bonfim and J. Florencio, *Phys. Rev. B* **74**, 134413 (2006).
- ³⁶ P. Fendley, *J. Phys. A* **52**, 335002 (2019).
- ³⁷ F. C. Alcaraz, R. A. Pimenta, and J. Sirker, *Phys. Rev. B* **107**, 235136 (2023).
- ³⁸ S. Y. Pang, S. V. Muniandy, and M. Z. M. Kamali, *Int. J. Theor. Phys.* **58**, 4139 (2019).
- ³⁹ P. Calabrese and J. Cardy, *J. Stat. Mech.* **P06002** (2004).
- ⁴⁰ P. Chen, Z.-L. Xue, I. P. McCulloch, M.-C. Chung, C.-C. Huang, and S.-K. Yip, *Phys. Rev. Lett.* **114**, 145301 (2015).
- ⁴¹ R. Dijkgraaf, E. Verlinde, and H. Verlinde, *Commun. Math. Phys.* **115**, 649 (1988).

- ⁴² J. Um, S.-I. Lee, and B. J. Kim, Journal of the Korean Physical Society **50**, 285 (2007).
- ⁴³ P. Zanardi, M. G. A. Paris, and L. Campos Venuti, Phys. Rev. A **78**, 042105 (2008).
- ⁴⁴ B. Damski, Phys. Rev. E **87**, 052131 (2013).
- ⁴⁵ K. Binder, Z. Phys. B **43**, 119 (1981).
- ⁴⁶ C. G. West, A. Garcia-Saez, and T.-C. Wei, Phys. Rev. B **92**, 115103 (2015).
- ⁴⁷ Y.-C. Wang, Y. Qi, S. Chen, and Z. Y. Meng, Phys. Rev. B **96**, 115160 (2017).
- ⁴⁸ A. W. Sandvik, AIP Conference Proceedings **1297**, 135 (2010).
- ⁴⁹ S. Jin, A. Sen, and A. W. Sandvik, Phys. Rev. Lett. **108**, 045702 (2012).
- ⁵⁰ S. Capponi, S. S. Jahromi, F. Alet, and K. P. Schmidt, Phys. Rev. E **89**, 062136 (2014).
- ⁵¹ K. Vollmayr, J. D. Reger, M. Scheucher, and K. Binder, Z. Phys. B **91**, 113 (1993).
- ⁵² D. Friedan, Z. Qiu, and S. Shenker, Phys. Rev. Lett. **52**, 1575 (1984).
- ⁵³ J. Ashkin and E. Teller, Phys. Rev. **64**, 178 (1943).
- ⁵⁴ N. Chepiga, SciPost Phys. Core **5**, 031 (2022).
- ⁵⁵ F. Y. Wu, Rev. Mod. Phys. **54**, 235 (1982).
- ⁵⁶ A. O'Brien, S. D. Bartlett, A. C. Doherty, and S. T. Flammia, Phys. Rev. E **92**, 042163 (2015).
- ⁵⁷ N. D. Chavda, H. N. Deota, and V. K. B. Kota, Phys. Lett. A **378**, 3012 (2014).
- ⁵⁸ Y. Y. Atas, E. Bogomolny, O. Giraud, and G. Roux, Phys. Rev. Lett. **110**, 084101 (2013).
- ⁵⁹ V. Oganesyan and D. A. Huse, Phys. Rev. B **75**, 155111 (2007).
- ⁶⁰ L. D'Alessio, Y. Kafri, A. Polkovnikov, and M. Rigol, Adv. Phys. **65**, 239 (2016).
- ⁶¹ F. Anza, C. Gogolin, and M. Huber, Phys. Rev. Lett. **120**, 150603 (2018).
- ⁶² R. Reuvers, Proc. R. Soc. A. **474**, 20180023 (2018).
- ⁶³ We thank Hosho Katsura for an observation which led to the analytical results presented in this section.
- ⁶⁴ L. Pauling, J. Chem. Phys. **1**, 280 (1933).
- ⁶⁵ B. Mukherjee, S. Nandy, A. Sen, D. Sen, and K. Sengupta, Phys. Rev. B **101**, 245107 (2020).
- ⁶⁶ S. Sugiura, T. Kuwahara, and K. Saito, Phys. Rev. Research **3**, L012010 (2021).
- ⁶⁷ B. Mukherjee, A. Sen, D. Sen, and K. Sengupta, Phys. Rev. B **102**, 075123 (2020).
- ⁶⁸ K. Mizuta, K. Takasan, and N. Kawakami, Phys. Rev. Research **2**, 033284 (2020).
- ⁶⁹ B. Mukherjee, A. Sen, D. Sen, and K. Sengupta, Phys. Rev. B **102**, 014301 (2020).
- ⁷⁰ B. Mukherjee, A. Sen, and K. Sengupta, Phys. Rev. B **106**, 064305 (2022).

Appendix A: Expectation values of local operators and duality for finite systems

In this appendix, we will study the expectation values of local operators in all the eigenstates of the Hamiltonian, and we will see that something striking occurs when the system has an exact self-duality. Let us write the Hamiltonian in Eq. (2) in the form shown in Eq. (8). It is then interesting to plot the expectation value of, say, X in the different eigenstates of H versus the energies of those states. If the system is integrable, we might expect to see a fragmented kind of pattern

corresponding to the different conserved sectors, while for a non-integrable system, we would not expect to see any special pattern.

It turns out that something interesting happens at the critical point $h = 1$. We have discussed in Sec. III that the system with L sites and PBC is self-dual only if L is not a multiple of 3. We therefore expect, from Eq. (11), that a plot of $\langle \psi_n | X | \psi_n \rangle$ versus E_n (where n denotes the eigenstate number) should be a perfect straight line with slope equal to $-1/2$ if L is not a multiple of 3. But if L is a multiple of 3, the self-duality does not hold and the plot is not expected to be a perfect straight line; we expect several points to lie away from the straight line. This is exactly what we see in Fig. 19. We see a perfect straight line for a system size $L = 13$ where there is exact self-duality but a scattering of points when $L = 12$ where the self-duality is not exact.

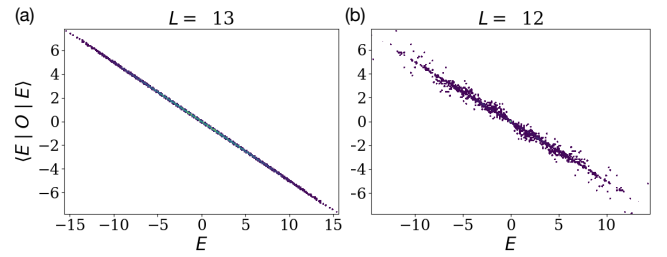


FIG. 19: (a) Expectation value of the operator $\langle \psi_n | X | \psi_n \rangle$ plotted as a function of the energy E_n , where ψ_n is the n -th energy eigenstate, for $h = 1$. We see that for a system size $L = 13$ which is not a multiple of three, the curve falls exactly a straight line with a slope of -0.5 . (b) The same plot for a system size $L = 12$ which is a multiple of three. We see that there is a scattering of the data points as the system no longer has exact self-duality.

Appendix B: Fourier transform of the autocorrelator A^{zz} for $h \geq 1$

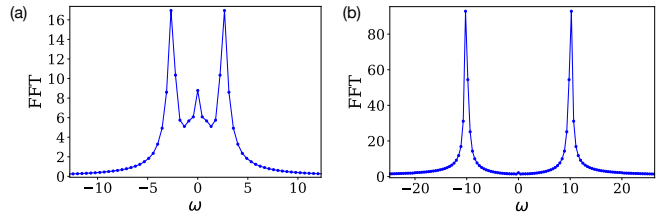


FIG. 20: (a) $\tilde{A}_{l=1}^{zz}(\omega)$ at $h = 1$ for a system with $L = 14$. (b) The same quantity at $h = 5$.

Here we present the plots for $\tilde{A}_{l=1}^{zz}(\omega)$ for $h = 1$ and 5, which are obtained by taking the Fourier transform of $A_{l=1}^{zz}(t)$ at those values of h over a large interval τ . More precisely,

$$\tilde{A}_{l=1}^{zz}(\omega) = \frac{1}{\tau} \int_{\tau_0}^{\tau_0+\tau} dt e^{-i\omega t} A_{l=1}^{zz}(t), \quad (\text{B1})$$

where the starting time τ_0 is chosen carefully to eliminate the

initial decay so that it can capture the oscillatory nature of the correlator. The time interval τ is taken to be large enough to contain a certain number of complete oscillations which provides a better resolution in the frequency space. Since the oscillations persisted more for larger h , the values of τ also was taken to be different for different values of h . In our case τ was chosen to be 15 for $h = 1$ and 20 for $h = 5$. The well-defined peaks denote the frequencies of oscillations of the au-

tocorrelator shown in Fig. 17. Moreover, the decays of the oscillations lead to a finite width around the peak of the Fourier transform which goes roughly as $1/h$. This is clear from the figure, as the width is much smaller for $h = 5$ (Fig. 20 (b)) than for $h = 1$ (Fig. 20 (a)). The small peak around $\omega = 0$ for $h = 1$ is because of the initial high value of the autocorrelator which adds to a constant value while performing the Fourier transform over a time interval.